Nonperturbative running of the quark mass for $N_f = 3$ QCD from the chirally rotated Schrödinger functional

Isabel Campos Plasencia,[1] Mattia Dalla Brida,[2] Giulia Maria de Divitiis,[3,4] Andrew Lytle,[5] Mauro Papinutto,[6] Ludovica Pirelli,[3,4] and Anastassios Vladikas[4]

(ALPHA Collaboration)

[1]*Instituto de Física de Cantabria IFCA-CSIC, Avenida de los Castros s/n, 39005 Santander, Spain*
[2]*Theoretical Physics Department, CERN, CH-1211 Geneva 23, Switzerland*
[3]*Dipartimento di Fisica, Università di Roma "Tor Vergata", Via della Ricerca Scientifica 1, 00133 Rome, Italy*
[4]*INFN, Sezione di Tor Vergata, Via della Ricerca Scientifica 1, 00133 Rome, Italy*
[5]*Department of Physics, University of Illinois at Urbana-Champaign, Urbana, Illinois 61801, USA*
[6]*Dipartimento di Fisica, Università di Roma La Sapienza, and INFN, Sezione di Roma, Piazzale Aldo Moro 2, 00185 Rome, Italy*

(Received 10 January 2022; accepted 22 February 2022; published 14 March 2022)

We study the renormalization group (RG) running of the quark mass, for $N_f = 3$ QCD with Wilson fermions in a mixed action setup, with standard Schrödinger functional (SF) boundary conditions for sea quarks and chirally rotated Schrödinger functional (χSF) boundary conditions for valence quarks. This necessitates the tuning of the boundary factor $z_f(g_0^2)$ of the χSF valence action, in order to ensure that QCD symmetries are fully recovered in the continuum. The properties of this novel setup are monitored through the ratios Z_S/Z_P and Σ_S/Σ_P of the renormalization parameters and step scaling functions of the scalar and pseudoscalar densities. Where comparison is possible, our Z_S/Z_P results are found to agree with previous determinations, based on a mass ratio method [G. M. de Divitiis *et al.* (ALPHA Collaboration), Eur. Phys. J. C **79**, 797 (2019)] and Ward identities [J. Heitger *et al.* (ALPHA Collaboration), Eur. Phys. J. C **80**, 765 (2020); J. Heitger *et al.*, Eur. Phys. J. C **81**, 606 (2021)], with Schrödinger functional boundary conditions. The behavior of Σ_S/Σ_P confirms the theoretical expectations of χSF QCD, related to the restoration of the theory's symmetries in the continuum limit. From the step-scaling function of the pseudoscalar density we obtain the quark mass RG-running function from hadronic to perturbative energy scales. This is fully compatible with the earlier result obtained in a similar setup for Wilson quarks with Schrödinger functional boundary conditions [I. Campos *et al.*, Eur. Phys. J. C **78**, 387 (2018)], and provides a strong universality test for the two lattice setups.

DOI: 10.1103/PhysRevD.105.054506

I. INTRODUCTION

The chirally rotated Schrödinger functional (χSF) [1] is a variant of the Schrödinger functional (SF) renormalization scheme, which enables us to obtain renormalization parameters and lattice step-scaling functions, which are "automatically" $O(a)$ improved.

At the formal level, continuum massless QCD with SF boundary conditions (SF-QCD) is equivalent to the one with χSF boundaries (χSF-QCD), as one is obtained from the other by suitable redefinitions of the fermion fields, which are nonanomalous chiral rotations in isospin space. These redefinitions also modify the form of the various symmetries of the theory in the χSF setup. In particular, standard parity $\mathcal{P}$ in SF-QCD is chirally rotated to the so-called $\mathcal{P}_5$ symmetry in χSF-QCD. When massless QCD is regularized with Wilson fermions, the strict equivalence between the theories with SF and χSF boundaries is lost. A consequence of this is that lattice QCD with SF boundaries (SF-LQCD) retains $\mathcal{P}$ symmetry, while its χSF counterpart (χSF-LQCD) is not $\mathcal{P}_5$ symmetric. The restoration of $\mathcal{P}_5$ in the continuum limit requires the introduction of a new counterterm at the time boundaries with a coefficient $z_f(g_0^2)$. The new counterterm must be tuned by imposing

that a $\mathcal{P}_5$-odd correlation function in χSF-LQCD vanishes. Once this is achieved (together with the tuning of the Wilson hopping parameter to κ_c, which ensures that fermions are massless), continuum limit universality implies that, at vanishing lattice spacing, $\mathcal{P}_5$-even, renormalized correlation functions in χSF-LQCD are equal to their $\mathcal{P}$-even counterparts in SF-LQCD. The same is true for $\mathcal{P}_5$-odd χSF-LQCD and $\mathcal{P}$-odd SF-LQCD correlation functions; being pure lattice artifacts, these vanish in the continuum.

In massless QCD with SF boundary conditions, $O(a)$ improvement is achieved through the introduction of Symanzik counterterms in the action, both in the lattice bulk (i.e., the clover term of the fermion action with its coefficient $c_{\rm sw}$) and at the time boundaries (i.e., the terms with coefficients $c_{\rm t}$ of the gauge action and $\tilde{c}_{\rm t}$ of the fermionic one) [2]. Composite operators inserted in the lattice bulk in correlation functions also require their own counterterms (e.g., c_A, c_V for the axial and vector nonsinglet currents respectively). The bulk improvement coefficients (e.g., $c_{\rm sw}, c_A, c_V$) are typically known nonperturbatively, whereas $c_{\rm t}$ and $\tilde{c}_{\rm t}$ are known in one- and sometimes in two-loop perturbation theory. This implies that $O(a)$ effects are removed in the bulk and $O(g_0^2 a)$ effects are removed from the time boundaries. In practice, the former have always been found to be dominant, in the sense that quantities thus improved scale like $O(a^2)$.

In massless QCD with χSF boundary conditions, bulk counterterms like, $c_{\rm sw}, c_A$ and c_V are in principle not required for the removal of bulk $O(a)$ effects in the quantities of interest [1] ("automatic improvement"). The only necessary boundary counterterms are $z_{\rm f}$ and d_s [which are $O(a^0)$ and $O(a)$ respectively] for the fermionic action and $c_{\rm t}$ [which is $O(a)$] for the gluonic one. We compute $z_{\rm f}$ nonperturbatively, while $c_{\rm t}$ is known at one-loop in perturbation theory. For d_s the tree-level value is adequate 1,3]]; this will be checked explicitly in this work. This leaves us with $O(a^2)$ effects in the bulk and effectively with $O(g_0^4 a)$ effects at the time boundaries. Provided the latter turn out to be subdominant, the scaling of our results should be compatible with $O(a^2)$.

Several tests have been performed, which confirm this expectation:

(i) In Ref. [4] automatic improvement was thoroughly investigated nonperturbatively in a quenched setup for lattices with $L = 1.436 r_0$, with r_0 the Sommer scale [5]. The tuning of $z_{\rm f}$ was shown to be done correctly by checking the vanishing of $\mathcal{P}_5$-odd χSF correlation functions in the continuum limit. Ratios of $\mathcal{P}_5$-even χSF correlation functions to their SF counterparts, which ought to have the same continuum limit, are indeed shown to be compatible with unity, scaling like $O(a^2)$, as they should.

(ii) In Ref. [3] analogous tests have been performed in perturbation theory at one-loop.

(iii) A second quenched study [6,7] was centred on the step-scaling functions of the pseudoscalar density and nonsinglet twist-2 operators at one intermediate and one perturbative scale. Moreover, the renormalization factor Z_P was computed at the scale $L = 1.436 r_0$. Combining Z_P with the bare twisted-mass parameter and the known ratio $M/\bar{m}(1/L)$ of Ref. [8], estimates of the strange quark mass were obtained. Comparison of results obtained with (i) unimproved SF Wilson fermions, (ii) SF clover fermions, and (iii) χSF fermions confirmed automatic improvement of the latter and the universality of the continuum limit.

(iv) In Ref. [9] these efforts have been extended to massless QCD with $N_f = 2$ and $N_f = 3$ dynamical flavors. In the $N_f = 3$ case, the light sea quark doublet has been regularized in χSF-LQCD and the third sea flavor in SF-LQCD.

A first goal of the present work is to pursue analogous tests from a different angle. We use the gauge ensembles of Ref. [10], generated for the nonperturbative determination of the renormalization group (RG) running of the quark mass in $N_f = 3$ massless QCD with SF boundaries. The renormalization scales μ cover a wide energy range $\Lambda_{\rm QCD} \lessapprox \mu \equiv 1/L \lessapprox M_W$. Here L denotes the lattice physical extension; note that it ranges from very small values of about $L \approx 10^{-3}$ to $L \lessapprox 1$ fm. On these ensembles we compute correlation functions with dimension-3 scalar and pseudoscalar bilinear operators in the bulk and χSF boundary conditions. This is a mixed action approach, as sea and valence quarks have different regularizations (SF and χSF respectively). So our whole setup is different than those listed above. Several new universality tests are then possible, using different χSF correlation functions which have the same continuum limit.

The main result of this work consists of an estimate of $M/\bar{m}(1/L)$ and its comparison to the one obtained in a SF setup in Ref. [10]. This is a first step in a project, which ultimately aims at providing nonperturbative improved estimates of the step-scaling matrices of all four-fermion operators that contribute to B_K in the Standard Model and beyond. This has already been done for $N_f = 2$, but in SF-LQCD [11,12]. Adopting a χSF-LQCD setup instead brings in automatic $O(a)$ improvement of the relevant dimension-6 operators and allows the introduction of renormalization schemes involving simpler correlation functions with better signal-to-noise behavior. The corresponding bare matrix elements are to be computed in twisted-mass LQCD at maximal twist (with Osterwalder-Seiler fermions), with the Clover term retained in the action, for reasons explained in Ref. [13]. For a first discussion of this strategy, the reader may consult Refs. [14,15].

This paper is organized as follows: Sec. II is an overview of the fundamental properties of the χSF lattice regularization with Wilson quarks and the basic definitions and properties of the quantities of interest. Section III describes the details of our numerical simulations. The results of the tuning of the χSF-LQCD factor z_f, essential for the recovery of all QCD symmetries in the continuum, is also presented. In Sec. IV we obtain results for the ratio Z_S/Z_P of the renormalization factors of the scalar and pseudoscalar bilinear operators. We find that the behavior of Z_S/Z_P at high energies agrees with expectations from perturbation theory; at low energies it agrees with earlier nonperturbative determinations, based on other methods. Moreover we confirm that the ratio $\Sigma_{S/P}$ of the corresponding step-scaling functions in the χSF theory goes to unity in the continuum limit, in accordance with chiral symmetry restoration. In Secs. V and VI we obtain results for the step-scaling function of the pseudoscalar bilinear operator in the high- and low-energy regimes of our simulations respectively. In each case we compute the RG running function between the lowest and highest energy in each of the two regimes. Our results agree with those of Ref. [10]. Finally, in Sec. VII we conclude by presenting the total RG-running factor between hadronic and very high (perturbative) scales. Several details of our analysis are treated separately in the Appendices. Our results have been presented in preliminary form in Refs. [15,16].

II. THEORETICAL CONSIDERATIONS

We now cover briefly those aspects of the χSF regularization of Refs. [1,3] which are most relevant to our work. At the formal level, the massless QCD action is invariant under general flavor and chiral transformations. In particular, it is invariant under the change of variables,

$$\psi = R(\pi/2)\psi', \qquad \bar{\psi} = \bar{\psi}' R(\pi/2), \tag{1}$$

where $\psi, \bar{\psi}$ and $\psi', \bar{\psi}'$ are doublets in isospin space [e.g., $\psi = (\psi_u \psi_d)^T$], related through the above chiral nonsinglet transformations with $R(\alpha) = \exp(i\alpha\gamma_5\tau^3/2)$. In the SF-QCD setup, lattices have finite physical volume $L^3 \times T$ (in the present work $T = L$), with fields obeying Dirichlet (periodic) boundary conditions in time (space). The former are defined at $x_0 = 0$ and $x_0 = T$ as follows:

$$\begin{aligned} P_+\psi(x)|_{x_0=0} &= 0, \qquad P_-\psi(x)|_{x_0=T} = 0, \\ \bar{\psi}(x)P_-|_{x_0=0} &= 0, \qquad \bar{\psi}(x)P_+|_{x_0=T} = 0, \end{aligned} \tag{2}$$

with projectors $P_\pm = (1 \pm \gamma_0)/2$. The chiral rotations (1) map the above conditions onto the χSF boundary conditions

$$\begin{aligned} \tilde{Q}_+\psi'(x)|_{x_0=0} &= 0, \qquad \tilde{Q}_-\psi'(x)|_{x_0=T} = 0, \\ \bar{\psi}'(x)\tilde{Q}_+|_{x_0=0} &= 0, \qquad \bar{\psi}'(x)\tilde{Q}_-|_{x_0=T} = 0, \end{aligned} \tag{3}$$

with projectors $\tilde{Q}_\pm = (1 \pm i\gamma_0\gamma_5\tau^3)/2$. Thus SF-QCD and χSF-QCD are equivalent theories, since one is obtained from the other by the redefinition of fermionic fields (1).

Given the equivalence of the two theories, it is hardly surprising that they share all symmetries: the well-known SF-QCD symmetries, once transcribed in terms of fields ψ' and $\bar{\psi}'$, are those of χSF-QCD. Flavor symmetry in its standard SF-QCD version [e.g., Eq. (2.15) of Ref. [3]] takes the form of Eqs. (2.16) and (2.17) of [3]; parity $\mathcal{P}$ [Eq. (2.18) of [3]] becomes $\mathcal{P}_5$ [Eq. (2.19) of [3]] in χSF-QCD. Charge conjugation is form invariant in the two versions. We note in passing that the parity operator $\mathcal{P}_5$ commutes with the boundary projectors $\tilde{Q}_\pm$.

Similar considerations apply to correlation functions. Following Ref. [3], we introduce, in χSF-QCD, a second flavor doublet $(\psi_{u'}\psi_{d'})^T$, with exactly the same properties as the original one. In SF-QCD the two point function with a pseudoscalar insertion $P^{ud}(x)$ in the bulk and a boundary operator $\mathcal{O}_5^{du}$ at $x_0 = 0$ is defined as

$$f_P = -\frac{1}{2}\langle P^{ud}\mathcal{O}_5^{du}\rangle_{(P_+)}. \tag{4}$$

Analogous quantities in χSF-QCD are

$$g_X^{f_1 f_2} = -\frac{1}{2}\langle X^{f_1 f_2}\mathcal{Q}_5^{f_2 f_1}\rangle_{(\tilde{Q}_+)}, \tag{5}$$

with $X^{f_1 f_2} = P^{f_1 f_2}$ or $X^{f_1 f_2} = S^{f_1 f_2}$, and $\mathcal{Q}_5^{f_2 f_1}$ the result of the boundary field rotations (1) on the operator $\mathcal{O}_5$. The allowed combinations of flavor indices are $(f_1, f_2) = (u, u'), (d, d'), (u, d), (d, u)$ (so that no disconnected diagrams arise). See Ref. [3] for more detailed explanations. The relations between these correlation functions are then

$$f_P = ig_S^{uu'} = -ig_S^{dd'} = g_P^{ud} = g_P^{du}. \tag{6}$$

The SF boundary-to-boundary correlation function

$$f_1 = -\frac{1}{2}\langle \mathcal{O}_5^{ud}\mathcal{O}_5'^{du}\rangle_{(P_+)} \tag{7}$$

(with the boundary operator $\mathcal{O}_5'^{du}$ defined at $x_0 = T$) and its χSF counterpart

$$g_1^{f_1 f_2} = -\frac{1}{2}\langle \mathcal{Q}_5^{f_1 f_2}\mathcal{Q}_5'^{f_2 f_1}\rangle_{(\tilde{Q}_+)} \tag{8}$$

are also related:

$$f_1 = g_1^{uu'} = g_1^{dd'} = g_1^{ud} = g_1^{du}. \tag{9}$$

The above properties, though trivial at the formal level, have nontrivial consequences once the lattice regularization with Wilson fermions (χSF-LQCD) is introduced. (Of the three lattice χSF-QCD versions proposed in Ref. [1], we use that of Ref. [3]; see Sec. 3.1 of the latter work for the definition of the action etc.) The Wilson term and boundary terms in χSF-LQCD induce the breaking of the rotated flavor symmetry [i.e., Eqs. (2.16) and (2.17) of [3]] and parity $\mathcal{P}_5$ [i.e., Eq. (2.19) of [3]]. However, a symmetry argument analogous to that introduced in twisted-mass QCD [17] holds in the present case [1,18], with the result that $\mathcal{P}_5$-even correlation functions of the χSF-LQCD theory, once renormalized, are $O(a)$ improved in the bulk. An important additional ingredient of the lattice formulation consists in the introduction of the following boundary terms in the action:

$$\begin{aligned}&\bar{\psi}(x)[\delta D_W]\psi(x)\\ &= (\delta_{x_0,0} + \delta_{x_0,T})\bar{\psi}(x)[(z_{\mathrm{f}} - 1) + (d_s - 1)a\mathbf{D}_s]\psi(x).\end{aligned} \tag{10}$$

The operator $\mathbf{D}_s$ is the Dirac-Wilson lattice operator, summed over the three spatial directions only [see Eq. (3.14) of Ref. [3]]. It is an improvement counterterm, which cancels boundary $O(a)$ effects, once the coefficient $d_s(g_0^2)$ is properly tuned. Moreover, the aforementioned symmetry-breaking pattern of χSF-LQCD necessitates the introduction of an additional $O(a^0)$ boundary operator with coefficient $z_{\mathrm{f}}(g_0^2)$, which must be appropriately tuned, in order for the rotated flavor and $\mathcal{P}_5$ symmetries to be recovered in the continuum. The tuning condition consists in finding, at finite lattice spacing (i.e., nonzero g_0^2), the value of z_{f} for which a $\mathcal{P}_5$-odd correlation function vanishes. Specifically we require that

$$g_A^{ud}(x_0)|_{x_0=T/2} = 0, \tag{11}$$

where the $\mathcal{P}_5$-odd g_A^{ud} is defined in Eq. (5), with $X = A_0$. The above tuning must be coupled to the requirement that the theory be massless; i.e., the hopping parameter κ must be tuned to its critical value κ_{c}. This can be achieved by requiring the vanishing of the current quark mass

$$m(g_0^2, \kappa_{\mathrm{c}})|_{x_0=T/2} = 0, \tag{12}$$

which in χSF-LQCD may be defined as [9]

$$m^{\chi\mathrm{SF}}(g_0^2, \kappa) \equiv \frac{\frac{1}{2}(\partial_0 + \partial_0^*)g_A^{ud}(x_0)}{2g_P^{ud}(x_0)}, \tag{13}$$

where ∂_0, ∂_0^* are forward and backward lattice derivatives respectively. Recall that in SF-LQCD, in standard ALPHA fashion, the current quark mass is defined by [8]

$$m^{\mathrm{SF}}(g_0^2, \kappa) \equiv \frac{\frac{1}{2}(\partial_0 + \partial_0^*)f_A(x_0) + ac_A\partial_0^*\partial_0 f_P(x_0)}{2f_P(x_0)}. \tag{14}$$

In the above f_A is the analog of Eq. (4), with A_0^{ud} replacing P^{ud}. In SF-QCD, κ is tuned to its critical value κ_{c} by requiring the vanishing of m^{SF}.

The SF and χSF renormalization conditions for the pseudoscalar and scalar operators are imposed in the usual manner [3,8]:

$$\frac{Z_P^{\mathrm{SF}}(g_0^2, L/a)f_P(T/2)}{\sqrt{f_1}} = \left[\frac{f_P(T/2)}{\sqrt{f_1}}\right]^{\mathrm{t.l.}}, \tag{15}$$

$$\frac{Z_P^{\chi\mathrm{SF}}(g_0^2, L/a)g_P^{ud}(T/2)}{\sqrt{g_1^{ud}}} = \left[\frac{g_P^{ud}(T/2)}{\sqrt{g_1^{ud}}}\right]^{\mathrm{t.l.}}, \tag{16}$$

$$\frac{Z_S^{\chi\mathrm{SF}}(g_0^2, L/a)g_S^{uu'}(T/2)}{\sqrt{g_1^{uu'}}} = \left[\frac{g_S^{uu'}(T/2)}{\sqrt{g_1^{uu'}}}\right]^{\mathrm{t.l.}}, \tag{17}$$

where the superscripts t.l. on the rhs stand for "tree level" (these tree-level quantities are computed at nonvanishing a/L). From them we determine the renormalization constants Z_P in the SF and χSF renormalization schemes and Z_S in the χSF scheme.

As a side remark we point out that standard parity $\mathcal{P}$, combined with flavor exchanges $u \leftrightarrow d$ and $u' \leftrightarrow d'$, is an exact symmetry of χSF-LQCD [1,3]. This ensures that $g_S^{uu'} = -g_S^{dd'}$ and $g_P^{ud} = g_P^{du}$ are exact lattice relations. For this reason we have not used the correlation functions $g_S^{dd'}$ and g_P^{du}, as they do not convey any new information.

The definitions of the lattice step-scaling functions (SSF) are also standard:

$$\Sigma_P^{\mathrm{SF}}(g_0^2, a/L) = \frac{Z_P^{\mathrm{SF}}(g_0^2, 2L/a)}{Z_P^{\mathrm{SF}}(g_0^2, L/a)}, \tag{18}$$

$$\Sigma_P^{\chi\mathrm{SF}}(g_0^2, a/L) = \frac{Z_P^{\chi\mathrm{SF}}(g_0^2, 2L/a)}{Z_P^{\chi\mathrm{SF}}(g_0^2, L/a)}, \tag{19}$$

$$\Sigma_S^{\chi\mathrm{SF}}(g_0^2, a/L) = \frac{Z_S^{\chi\mathrm{SF}}(g_0^2, 2L/a)}{Z_S^{\chi\mathrm{SF}}(g_0^2, L/a)}. \tag{20}$$

On the lattice, SF-QCD and χSF-QCD are two regularizations of the same continuum theory, in which the pseudoscalar and scalar operators belong to the same symmetry multiplets (such as the chiral multiplet) and thus have the same anomalous dimension. Consequently, the above SSFs should have the same continuum limit:

$$\sigma_P(u) = \lim_{a\to 0}\Sigma_X^Y(g_0^2, a/L)|_{\bar{g}^2(L)=u}. \tag{21}$$

In the above $(X, Y) = (P, \mathrm{SF})$, $(P, \chi\mathrm{SF})$, $(S, \chi\mathrm{SF})$. The squared renormalized coupling $\bar{g}^2(L)$ is meant to be held fixed at a value u while the continuum limit is taken. In terms of the renormalized quark mass $\bar{m}(\mu)$, defined at a scale $\mu = 1/L$, which corresponds to a renormalized coupling $\bar{g}^2(\mu) = u$, the continuum step-scaling function is given by the ratio

$$\sigma_P(u) = \frac{\bar{m}(\mu)}{\bar{m}(\mu/2)}. \tag{22}$$

So far we have dealt with SF-QCD and χSF-QCD as two distinct, if related, setups. As noted in Ref. [1], for an odd number of flavors, the fermion determinant in the χSF formalism is in general complex. For $N_f = 3$ QCD the problem has been circumvented in Ref. [9] by working with a χSF-LQCD light sea quark doublet and a SF-LQCD third sea flavor. Here we adopt a different mixed action approach, with the sea quark action obeying standard SF boundary conditions, and the valence quark action defined for an even number of fermions obeying χSF boundary conditions. For the sea quarks, we use the existing SF-QCD configuration ensembles of Ref. [10]. The novelty with respect to Ref. [10] thus consists in having valence fermions organized in doublets with χSF boundary conditions. Apart from this, the lattice gauge action, the fermion action in the lattice bulk (Wilson fermions with a clover term), and the renormalized coupling definition(s) remain the same. Since our lattice valence quark propagators are now computed in a χSF setup, it is χSF symmetries that determine the renormalization and improvement properties of the correlation functions and the quantities derived from them. Thus we expect $O(a)$ improvement to be automatic in the bulk (i.e., in general bulk operators do not require Symanzik coefficients, e.g., c_A and c_T for the axial and tensor bilinears).

In this setup we use renormalization conditions (16) and (17) for the computation of Z_P and Z_S and definitions (19) and (20) for the SSFs. The three SSFs, computed from (18) * in Ref. [10] and Eqs. (19) and (20) in this work, should yield the same SSF σ_P in the continuum, since the same renormalization conditions are imposed.

In a purely χSF-LQCD setup, the necessary tuning of z_f is based on Eq. (11), while that of κ on Eqs. (12) and (13). In practice the tuning of the two parameters can be done independently, as they depend weakly on each other [9]. In our mixed action setup, we avoid tuning κ altogether, as we can use the κ_c results of Ref. [10], which are based on Eq. (14). Moreover, the tuning of z_f is performed exclusively in the valence sector, given that our sea SF-QCD quarks are "blind" to this factor. This is to be contrasted to the much costlier z_f tuning in the purely χSF-LQCD case, where the generation of the gauge ensembles depends on z_f.

III. NUMERICAL SIMULATIONS

We have seen in Sec. II that sea quarks are regularized as explained in Ref. [10]. For this reason, the first part of this section consists in a recapitulation of aspects of that work which are relevant to the present one.

The lattice volumes L^4 in which simulations are performed define the range of accessible energy scales $\mu = 1/L$. Essentially there are two energy regimes. The high-energy one concerns scales in the range $\mu_0/2 \lessapprox \mu \lessapprox M_W$, with an intermediate ("switching") scale conventionally chosen to be $\mu_0/2 \sim 2$ GeV. The low-energy regime concerns scales in the range $\Lambda_\mathrm{QCD} \lessapprox \mu \lessapprox \mu_0/2$. The main difference between the two [19–21] is the definition adopted for the renormalized coupling $\bar{g}$: in the high-energy range it is the nonperturbative SF coupling first introduced in Refs. [22,23]; in the low-energy one it is the gradient flow (GF) coupling defined in Ref. [24]. This allows to optimally exploit the variance properties of the couplings, so that a very precise computation of the Callan-Symanzik β function and ultimately of Λ_QCD is achieved [25].

In Refs. [19–21], the switching scale, $\mu_0/2$, where we switch between the SF and GF definitions of the coupling, was given implicitly by the formula

$$\bar{g}^2_\mathrm{SF}(\mu_0) \equiv u_{SF}(\mu_0) = 2.0120, \tag{23}$$

corresponding to the largest value for the renormalized coupling on the SF ensembles used in the analysis. The value of the SF coupling was determined down to the scale $\mu_0/2$ in [19]; this amounts to computing the SSF of the SF coupling

$$\sigma_\mathrm{SF}(u_0) \equiv \bar{g}^2_\mathrm{SF}(\mu_0/2) = u_{SF}(\mu_0/2) = 2.452(11). \tag{24}$$

The matching between schemes was subsequently specified by determining the value of the GF coupling at the same scale [20]:

$$\bar{g}^2_\mathrm{GF}(\mu_0/2) = u_{GF}(\mu_0/2) = 2.6723(64). \tag{25}$$

In physical units this corresponds to a switching scale $\mu_0/2$ of approximately 2 GeV [25].

Moreover, different lattice regularizations were adopted in each energy regime. At high energies, simulations were carried out using the plaquette gauge action [26] and the clover fermion action [27] with the nonperturbative value of c_sw [28] and the one- [29] and two-loop [30] values of $\tilde{c}_\mathrm{t}$ and c_t respectively. At low energies the tree-level Symanzik improved (Lüscher-Weisz) gauge action was used [31]. The fermion action was the $O(a)$-improved clover [27], with the nonperturbative value of the improvement coefficient c_sw [32] and one-loop values of $\tilde{c}_\mathrm{t}$ [20,33] and c_t [34].

Note that in Ref. [10] the same SF renormalization condition was used in both energy regimes for the determination of the quark mass renormalization factor $1/Z_P$, its

step-scaling function etc. This implies that σ_P and $\bar{m}$ are expected to be continuous functions of the renormalization scale μ in the whole simulation range $[\Lambda_{\rm QCD}, M_W]$. The same quantities, when plotted against the squared renormalized coupling u, will be discontinuous at the u value corresponding to the switching scale $\mu_0/2$, due to different definitions of the coupling below and above this scale. Any quantity is also going to be a discontinuous function of the squared inverse bare coupling β, as the bare actions are different in the two regimes.

At high energies, simulations were carried out [10] for eight values of the squared renormalized coupling $u_{\rm SF}$. For each of these couplings, corresponding to a fixed renormalization scale $\mu = 1/L$, the inverse bare coupling $\beta = 6/g_0^2$ was tuned appropriately for $L/a = 6, 8, 12$ (a is the lattice spacing). At the strongest coupling $u_{\rm SF} = 2.012$ of this high-energy range, an extra finer lattice with $L/a = 16$ was simulated. At low energies, simulations were carried out for seven values of the squared renormalized coupling u_{GF}. The inverse bare coupling $\beta = 6/g_0^2$ was chosen so that u_{GF} remains *approximately* constant for the three lattice volumes $L/a = 8, 12, 16$. In both the high and the low-energy ranges, gauge ensembles were generated at each $(\beta, L/a)$ and $(\beta, 2L/a)$ combination. At fixed $(\beta, L/a)$ the hopping parameter κ was tuned to its critical value $\kappa_{\rm c}$, so that the bare $O(a)$-improved partially conserved axial current (PCAC) mass defined in Eq. (14) vanishes at the corresponding value of β; cf. Eq. (12). For each $(\beta, L/a, \kappa_{\rm c})$ and $(\beta, 2L/a, \kappa_{\rm c})$ the factors $Z_P^{\rm SF}(g_0^2, L/a)$ and $Z_P^{\rm SF}(g_0^2, 2L/a)$ were computed using Eq. (15). Their ratio gives the SSF $\Sigma_P^{\rm SF}$ defined in Eq. (18). More details can be found in Ref. [10] and the Tables 6 and 9 (SF range) and 8 and 10 (GF range) of that work.

So far we have recapitulated the simulations of Ref. [10], performed in $N_f = 3$ QCD with sea and valence quarks subjected to SF boundary conditions. In the present work, we use the same configuration ensembles, with the exception of some β's where a few subsets of configurations could not be recovered; no significant loss in statistical accuracy resulted from this. We invert the Dirac-Wilson operator with χSF boundary conditions. Consequently $z_{\rm f}$ has to be determined so that Eq. (11) is satisfied. The results of $z_{\rm f}$ as a function of β for both high- and low-energy regimes are displayed in Fig. 1. It should be stressed that determining $z_{\rm f}$ is essential in order to ensure that in our mixed action approach chiral and flavor symmetries are recovered in the continuum and thus the theory belongs to the same universality class as other lattice regularizations. This is corroborated by the results of Sec. IV.

Details of the tuning procedure leading to $z_{\rm f}$ are discussed in Appendix A. As stated in Sec. II, the tuning of $z_{\rm f}$ must in principle be coupled with that of κ for the theory to be massless. This is not so in the procedure outlined above and in Appendix A, where we used the $\kappa_{\rm c}$

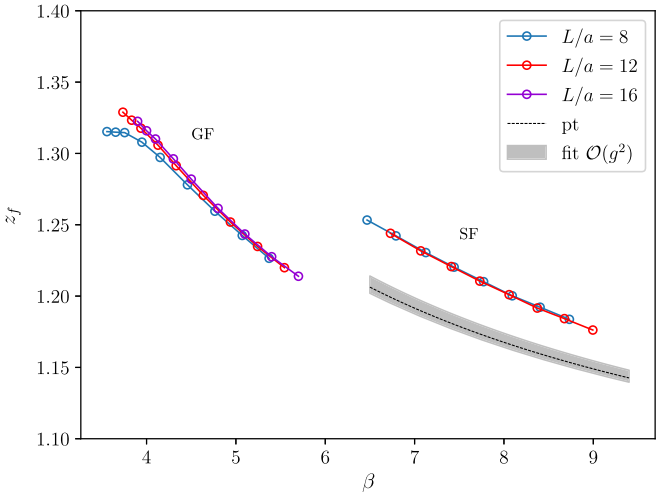

FIG. 1. The boundary counterterm $z_{\rm f}$ on the high energy (SF) and low-energy (GF) ensembles. The black dotted line is the perturbative result known at $O(g_0^2)$. The gray band is the result from fitting the SF data, plotted after the resulting expression has been truncated at $O(g_0^2)$ (i.e., the fit to the data correctly reproduces the perturbative prediction).

estimates of Ref. [10], based on the SF quark mass definition of Eq. (14). In the χSF setup the PCAC quark mass, defined by Eq. (13), is not expected to be exactly zero when $\kappa_{\rm c}$ is tuned in SF-LQCD. [The difference however is an $O(a)$ cutoff effect which induces $O(a^2)$ corrections in $\mathcal{P}_5$-even quantities.] One would expect that an iterative procedure in which $z_{\rm f}$ and κ are alternatively tuned would be needed. Such a procedure is adopted in Appendix B, where it is demonstrated that the tuning of $\kappa_{\rm c}$ alongside that of $z_{\rm f}$ is not necessary in practice.

The counterterm d_s, introduced in Eq. (10), is known at tree level [1] and, for the plaquette action, also at one-loop order [3]:

$$d_s = \frac{1}{2} + d_s^{(1)} g_0^2, \tag{26}$$

where

$$d_s^{(1)} = -0.0006(3) \times C_F. \tag{27}$$

For the Lüscher-Weisz action $d_s^{(1)}$ is not known at present. In Appendix C it is explicitly shown that results are unaffected when the one-loop estimate of d_s is used instead of its tree-level value.

For global fits throughout this work we use the LSQFIT [35] and GVAR [36] packages for correlated fitting and error propagation. We have checked that these results are consistent with jackknife and the Γ-method error analysis of Ref. [37]. Except for the last method, data have been binned by 20 configurations. The code to compute the χSF

correlation functions is built on OPENQCD 1.0 and previously used in Ref. [9].

In order to facilitate the future use of our χSF/SF-LQCD setup, we have gathered all relevant simulation details in Appendix D. These are the number of measurements $N_{\rm ms}$ for each ensemble, the lattice size L/a, the bare parameters $\beta, \kappa_{\rm c}$, the action coefficients $c_{\rm sw}, z_{\rm f}$, the renormalized squared coupling u, and the functions g_A^{ud} and $\partial g_A^{ud}/\partial z_{\rm f}$ used for the tuning of $z_{\rm f}$.

IV. THE RATIO Z_S/Z_P

Now we turn to the ratio of renormalization factors Z_S/Z_P. In Wilson formulations of lattice gauge theory, it is a finite quantity that depends on the bare gauge coupling,

$$\frac{Z_S}{Z_P} \simeq 1 + \sum_{i=1,j=0}^{\infty} c_{ij} g_0^{2i} \left(\frac{a}{L}\right)^{2j}. \tag{28}$$

In the $g_0 \to 0$ limit the above expression would be written as an equality, if terms containing products like $[a/L]^{2j}[\ln(a/L)]^k$ $(j > 0,\ k > 1)$ were also added to the series; cf. Eq. (7.4) of Ref. [3]. We drop these terms, which are habitually neglected, as they cannot be resolved by the data. We have also ignored nonperturbative contributions depending on $a\Lambda_{\rm QCD}$. We use the above expression for analyzing Z_S/Z_P in the high-energy region. At a fixed bare coupling there is a finite $a/L \to 0$ limit, and for our lattice setup the leading coefficient c_{10} has been calculated in lattice perturbation theory, $c_{10} = 0.025944(3)$ [3].

Unlike the renormalization factors Z_S and Z_P themselves, their ratio does not depend on the scale μ. Its continuum limit is known to be unity. Moreover, it has been calculated by other methods in the low-energy range for our lattice setup. Therefore it is suitable for some cross-checks of our results. Following Ref. [3], we compute Z_S/Z_P from the ratio

$$R_{\rm SP}^g \equiv \frac{g_P^{ud}(T/2)}{i g_S^{uu'}(T/2)} = \frac{Z_S}{Z_P} + O\left(\frac{a^2}{L^2}\right). \tag{29}$$

Note that $O(a)$ boundary effects cancel in this ratio, leaving us with $O(a^2)$ uncertainties.

In Fig. 2 we show data for Z_S/Z_P in the high-energy regime, where contact is made with perturbation theory. Due to the high degree of statistical correlation between $g_P^{ud}(x_0)$ and $g_S^{uu'}(x_0)$, the error bars are extremely small, of order 10^{-5} (as compared to 10^{-3} for the correlators individually). Nevertheless we are able to fit the data, performing global fits according to Eq. (28), provided enough terms in g_0^2 are retained. The coefficient c_{10} is kept fixed at its perturbative value and the series is truncated at $(i, j) = (5, 2)$. The goodness of the fit is $\chi^2/\text{d.o.f.} \sim 0.68$. Thus the numerical results appear to be joining smoothly onto the one-loop perturbative result at small bare coupling.

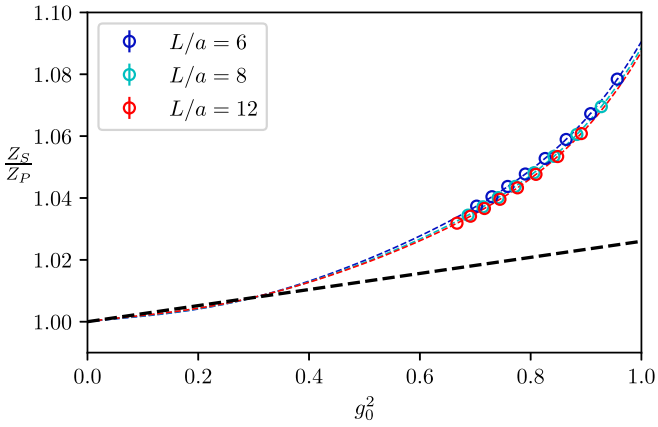

FIG. 2. The ratio Z_S/Z_P in the high-energy (SF) regime. The colored circles show our numerical data, and the colored dotted lines show the results of the fit to Eq. (28) evaluated at the respective L/a values. The black dotted line gives the $O(g_0^2)$ perturbative result.

If the term c_{10} is allowed to vary, the fit returns $c_{10} = 0.073(57)$ and $\chi^2/\text{d.o.f.} = 0.66$, compatible at 1σ with the perturbative value, but only weakly constrained. The three fit results for fixed $L/a = 6, 8, 12$ are shown as dashed lines in Fig. 2. Although they lie extremely close to each other, they are clearly distinct curves. These differences imply that finite size effects are tiny. This analysis has not been carried out along lines of constant physics; $O(a^2\Lambda_{\rm QCD}^2)$ effects have been neglected. It therefore probes the validity of perturbative expectations in a wide range of high-energy scales.

At low energies (GF) we show results for Z_S/Z_P in Fig. 3, and compare them with recent results obtained in [38] from suitable ratios of current and subtracted quark masses at two lines of constant physics (LCP-0,1) and in [39,40] using Ward identities (WI). These works use the same bulk action as the present one, with Schrödinger functional boundary conditions; quark masses lie close to

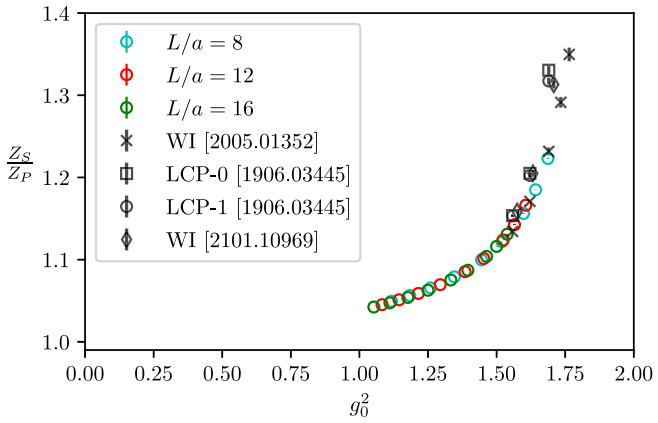

FIG. 3. The ratio Z_S/Z_P in the low-energy (GF) regime. Data is compared with the results of [38] using quark-mass ratio methods (LCP-0,1) and [39,40] obtained from Ward identities (WI).

the chiral limit; gauge couplings straddle the range of values of coordinated lattice simulations [41,42] suitable for the computation of low-energy hadronic quantities. Our results are compatible with those of the other methods in the infrared. The comparison of results from [38] and [39,40] was discussed already in [39,40], and it was observed that the WI method has smaller lattice artifacts. This can be expected to translate to an improved control of the continuum extrapolation of the quantities requiring Z_S/Z_P. Our results feature almost no visible finite volume effects and coincide numerically with the ones from [39] in the region of g_0^2 where they overlap. At g_0^2 values larger than about 1.6, different methods give slightly different results, signalling the presence of sizable discretization effects.

Besides the ratio Z_S/Z_P, we also examine the ratio of the corresponding SSF's $\Sigma_{P/S} \equiv \Sigma_P/\Sigma_S$. This is also a scale-independent quantity which becomes unity in the continuum limit. Once again, $O(a)$ boundary effects cancel in this ratio, leaving us with $O(a^2)$ uncertainties. This quantity is particularly suitable for studying universality.

We use $\Sigma_{P/S}$ in order to monitor the size of perturbative discretization effects, making use of lattice perturbation theory to $O(g_0^2)$; clearly this is meaningful only at high-energy (SF) scales. We first define the ratio of the lattice SSF $\Sigma_P(u, a/L)$, computed at one-loop, to the same quantity in the $L/a = \infty$ limit, in order to determine the numerical effect of all lattice artifacts appearing at this order:

$$\frac{\Sigma_P^{\text{1-loop}}(u, a/L)}{\sigma_P^{\text{1-loop}}(u)} = 1 + u\delta_P(a/L), \tag{30}$$

$$\delta_P(a/L) = -d_0 \ln(2) c_P(a/L). \tag{31}$$

In the above $d_0 = 8/(4\pi)^2$ is the universal anomalous dimension coefficient for the pseudoscalar bilinear operator. Analogous expressions are defined for the scalar operator (same d_0). The numerical values of $c_{S,P}(a/L)$, calculated in Ref. [43], are given in Table I.

The lattice artifacts of $O(g_0^2 a^n)$ are subsequently subtracted from the $\Sigma_{\text{S,P}}$ functions, computed nonperturbatively as in Eqs. (19) and (20), according to

TABLE I. Subtraction coefficients used to remove discretization effects from the nonperturbative step-scaling functions $\Sigma_{\text{S,P}}$ up to $O(g^2)$ as given in Eqs. (30) and (31).

L/a	$c_S(a/L)$	$c_P(a/L)$
6	0.1080	0.0486
8	0.0688	0.0458
12	0.0240	0.0168
16	0.0121	0.0086

$$\Sigma_{S,P}^{\text{sub}}(u, a/L) \equiv \frac{\Sigma_{S,P}(u, a/L)}{1 + u\delta_{S,P}(a/L)}. \tag{32}$$

The remaining discretization errors in $\Sigma_{S,P}^{\text{sub}}$ are $O(g_0^4 a^2)$.

Suppressing all $O(g_0^2 a^n)$ terms using lattice perturbation theory, we can in principle remove the corresponding parameters in our global fit ansatze; cf. Eq. (33). This means that we can expect more accurate determination of the remaining parameters, and more robust determinations e.g., upon increasing the order at which the expansion is truncated. Furthermore we might expect, especially at high energies where the gauge coupling is small, that removing lattice artifacts up to this order removes the largest contribution at each fixed order in a^n. This means that we may expect smaller coefficients in the remaining power series after the subtraction (i.e., the resulting power series is better behaved), although this is not guaranteed. Thus we would expect our fit forms, which are truncated to some order, to represent the subtracted data more accurately, resulting in better χ^2/d.o.f. and improved confidence in our extrapolated results:

$$\Sigma_{P/S}(u, a/L) = 1 + \sum_{i,j=1} d_{ij} u^i \left(\frac{a}{L}\right)^{2j}, \tag{33}$$

where terms depending on $\ln(a/L)$ are again neglected.

Here we test these expectations for the ratio of step-scaling functions $\Sigma_{P/S}$. Since the scalar and pseudoscalar bilinear operators have the same continuum anomalous dimension, the deviation of this quantity from 1 is a measure of lattice artifacts. For a fixed renormalized coupling u, the data should extrapolate to 1 in the $a/L \to 0$ limit. Figure 4 shows $\Sigma_{P/S}$ vs $(a/L)^2$ for the eight renormalized couplings in the high-energy (SF) regime, both before and after the subtraction specified by Eq. (32). The strong statistical correlation of Σ_P and Σ_S on a given

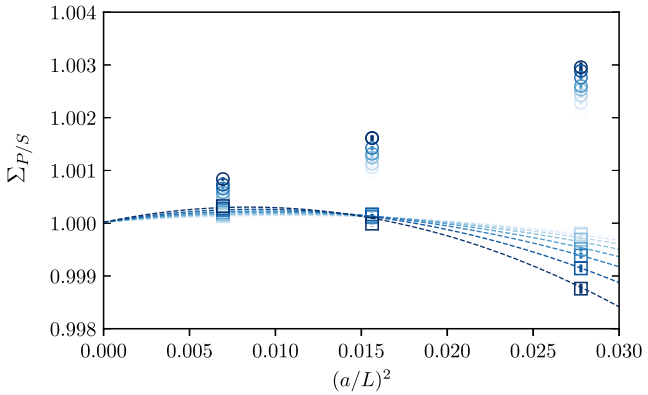

FIG. 4. Global fit of $\Sigma_{P/S}$ data in the high-energy (SF) regime after subtraction of $O(u, (a/L)^n)$ effects. Data before/after subtraction are given by open circles/squares. Fit results to the subtracted data are shown as dashed lines.

ensemble results to extremely small statistical uncertainty, leaving systematic effects to dominate. The raw data is shown above (circles, without lines passing through them), with the darker colors corresponding to larger renormalized coupling. We observe that the data at smaller coupling is nearer to 1, as is expected for a "well-behaved" series at small coupling and sufficiently small lattice spacing. A fit of the data to Eq. (33) for $(i,j)=(3,2)$ gives a $\chi^2/\text{d.o.f.}\sim 0.48$. Increasing $i_{\max}$ or $j_{\max}$ in the fit does not appreciably improve the $\chi^2/\text{d.o.f.}$

The lower part of Fig. 4 gives the same data but after subtraction specified by (32), along with the curves determined by a global fit to this data. For $L/a=8$ and 12, the subtracted data is exceptionally close to 1, indicating that the $O(g_0^2)$ lattice artifacts are indeed dominant. There is a more obvious discrepancy from 1 for $L/a=6$, up to around 0.001 for the $u=2.0120$ ensemble, but the overall size of this is significantly smaller than for the unsubtracted data, indicating the leading source of artifacts is still removed. Note that after subtraction the data at smaller coupling is still closer to 1 than the data at larger coupling. We can fit the subtracted data to the form Eq. (33), but now excluding the terms d_{1j} that should be absent from the subtraction. For the same $(i,j)=(3,2)$ fit as in the unsubtracted case, we find a $\chi^2/\text{d.o.f.}$ of 0.96. This is shown as the dotted lines in Fig. 4. As expected, we note that increasing $(i_{\max},j_{\max})$ improves the $\chi^2/\text{d.o.f.}$ somewhat and that fits to the unsubtracted data using the restricted form $d_{1j}=0$ result in poor χ^2.

The analogous study of the ratio Σ_P/Σ_S in the low-energy regime, shown in Fig. 5, does not involve any perturbative subtractions. The results reveal that higher order powers of $(a/L)^2$ are present, and become increasingly pronounced, at larger coupling. In fact, at our two largest couplings ($u=5.8673$ and $u=6.5489$), a low-order polynomial in $(a/L)^2$ has trouble capturing the behavior, indicating that in Σ_S or Σ_P (or both) an extrapolation to the continuum value may be unreliable for the given lattice extents and couplings. The result of fitting the data to Eq. (33) for $(i_{\max},j_{\max})=(4,3)$ is shown in Fig. 5, which returns a $\chi^2/\text{d.o.f.}$ of 4.2. Increasing $(i_{\max},j_{\max})$ improves the $\chi^2/\text{d.o.f.}$ somewhat, but all fits studied have trouble with the $L/a=8$ points for large coupling. On the other hand the (4,3) fit has $\chi^2/\text{d.o.f.}=1.3/0.66$ if data from the last/second to last couplings are removed.

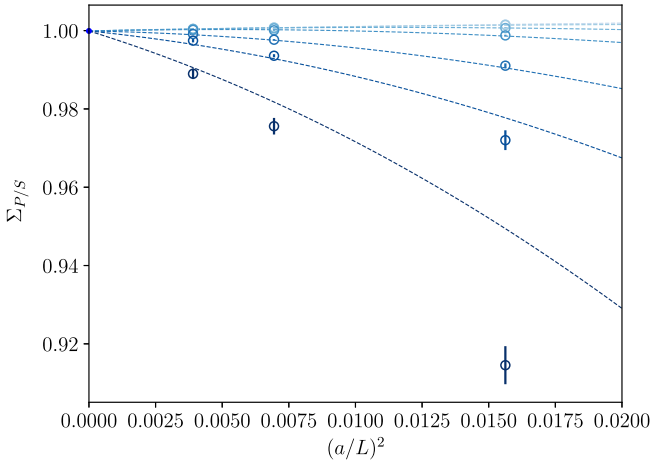

FIG. 5. Global fit of $\Sigma_{P/S}$ data in the low-energy (GF) regime.

V. QUARK MASS RUNNING AT HIGH ENERGIES

We now turn to the computation of the step-scaling functions themselves, which are the main inputs for the determination of the nonperturbative running of the quark masses. On each pair of $(L,2L)$ ensembles we compute $\Sigma_P^{\chi\text{SF}}$, defined in Eq. (19); henceforth the superscript χSF will be dropped:

$$\Sigma_P(u,a/L)=\frac{Z_P(u,2L/a)}{Z_P(u,L/a)}. \tag{34}$$

In both the high-energy and low-energy regimes we work at three different lattice spacings, except for the largest coupling in the high-energy range (the switching point, $u=2.0120$) where we use four lattice spacings. We note here that the values of Σ_P at different couplings are statistically uncorrelated. Furthermore the numerator and denominator are uncorrelated and as a result the statistical uncertainties are significantly larger than for the quantities $\Sigma_{P/S}$ or Z_S/Z_P studied in Sec. IV. In order to effectively leverage the data in the high-energy (SF) regime, we carry out a global to the following form:

$$\Sigma_P(u,a/L)=1+\sum_{i=1,j=0} b_{ij}u^i(a/L)^{2j}. \tag{35}$$

The continuum step-scaling function σ_P is then given by $\sigma_P(u)=\lim_{a\to 0}\Sigma_P(u,a/L)$. Although $\Sigma_P(g_0^2,a/L)$ is computed at specific values of the bare coupling and lattice volume, we are interested in its behavior with varying renormalized coupling; hence the notation $\Sigma_P(u,a/L)$.

The continuum coefficient $b_{10}=-d_0\ln(2)$ is known from perturbation theory, where $d_0=8/(4\pi)^2$ is the universal lowest-order quark mass anomalous dimension; see Eq. (39) below. Also known in perturbation theory is the coefficient $b_{20}=-d_1\ln(2)+(d_0^2/2-b_0d_0)\ln(2)^2$. Here $b_0=(11-2N_f/3)/(4\pi)^2$ is the universal lowest-order coefficient of the Callan-Symanzik β function and $d_1=1/(4\pi)^2(0.2168+0.084N_f)$, the next-to-leading order coefficient of the quark mass anomalous dimension, is specific to the SF scheme and was computed in [44]. For $N_f=3$ we have $b_{20}=-0.0028$. We can constrain the fit form Eq. (35) using these values. By subtracting leading $O(u)$ discretization errors from our data [cf. Eq. (32)], we

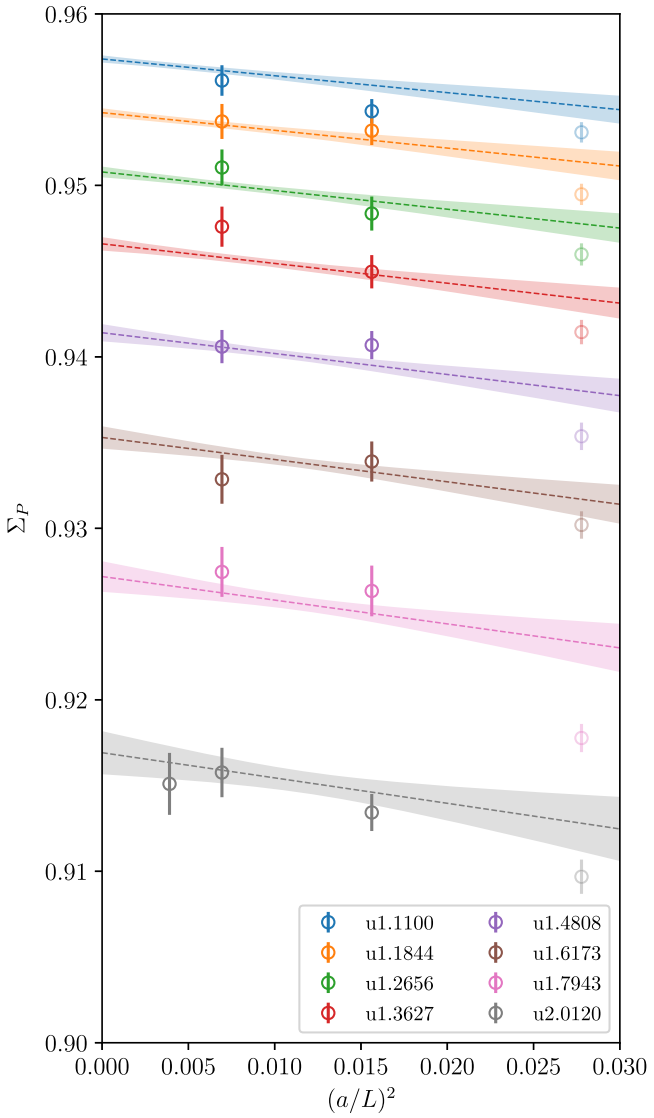

FIG. 6. Results of a global fit to the step-scaling data $\Sigma_P(u, a/L)$ in the high-energy regime. The open circles give the raw data while the filled bands are the results returned from the fit at the respective u values. The transparent $L/a = 6$ data points are not included in the fit. The data points and the bands of the same color are at a fixed value of the renormalized squared coupling u.

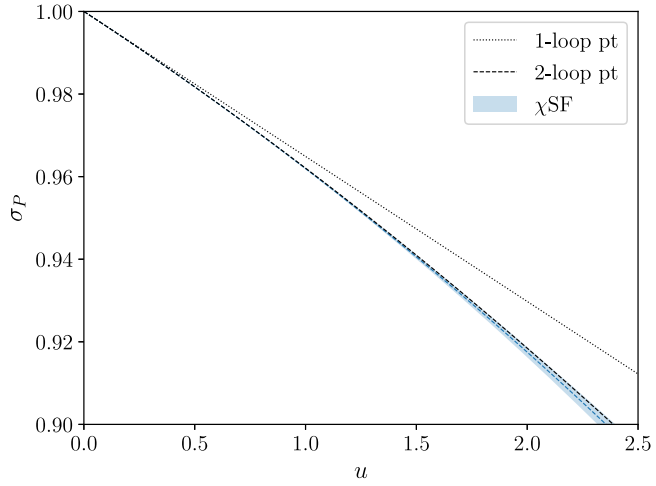

FIG. 7. Continuum limit of the nonperturbatively determined step-scaling function $\sigma_P(u)$, compared with perturbation theory. The one-loop perturbative result is universal while the two-loop result is specific to the (χ)SF renormalization scheme.

can also set the terms $b_{1j>0}$ to zero. However we find that doing so generally leads to somewhat higher χ^2/d.o.f. values (and is less conservative, giving smaller errors), and so we choose to work with the unsubtracted data.

For the fits considered here we take $(i_{\max}, j_{\max}) = (3, 2)$. When fitting the full dataset, we find χ^2/d.o.f. ≈ 1.4, and this is not appreciably improved by increasing $(i_{\max}, j_{\max})$. We attribute this to a partial breakdown of the polynomial form Eq. (35) when including the $L/a = 6$ points in our dataset, especially at large couplings. If we remove these points we find an improved χ^2/d.o.f. $= 0.95$. If we leave the term b_{20} unconstrained this fit returns a value of $b_{20} = -0.0019(11)$, compatible with the perturbative value. Including the $L/a = 6$ data instead gives $b_{20} = -0.0012(9)$, once again giving some evidence that the form (35) strains to represent these points. Therefore for our preferred fit we drop the $L/a = 6$ data and fix b_{20} to its perturbative value.

The raw step-scaling data in the high-energy regime, along with the curves from the global fits evaluated at their respective u values, are shown in Fig. 6.

The continuum curve $\sigma_P(u)$ obtained from the fit (35) is shown in Fig. 7 and compared with the expectations from perturbation theory. One sees that in the high-energy region the nonperturbative result agrees well with the two-loop result from perturbation theory, indicating that the perturbative series is fairly well converged. This result is also consistent with the findings of [10], and demonstrates the universality of χSF and SF.

We have established that the result shown in Fig. 7 is a robust nonperturbative estimate of $\sigma_P(u)$. Having been constrained by perturbation theory at small couplings, it is also valid below the lowest simulated value $u_{\mathrm{SF}} \sim 1.1$. In other words, this result can be used in the whole energy range above $\mu_0/2 \sim 2$ GeV, allowing us to compute the mass-evolution values $R^{(k)}$, defined as [cf. Eq. (22)]

$$R^{(k)} = \frac{\bar{m}(2^k\mu_0)}{\bar{m}(\mu_0/2)} = \prod_{n=0}^{k} \sigma_P(u_n), \tag{36}$$

for arbitrarily large energy scales $2^k\mu_0$ (large k); in the above $u_n = u_{\mathrm{SF}}(2^n\mu_0)$. For small values of k, Table II shows our results for $R^{(k)}$ from the fit to the full dataset (labeled $R^{(k)}$) and those excluding the $L/a = 6$ data points (labeled $R^{(k)}$-w/o 6). The results including the $L/a = 6$ data are systematically larger than those without, an effect

TABLE II. Mass ratios $R^{(k)}$, obtained from nonperturbative SSF in χSF for increasing k values, compared with the preferred SF fit from Ref. [10]. The column marked $R^{(k)}$-w/o 6 gives results excluding the $L/a = 6$ data points in the fit.

k	u_k	$R^{(k)}$-w/o 6	$R^{(k)}$	$R^{(k)}$ [10]
0	2.0120	0.9169(13)	0.9191(10)	0.9165(12)
1	1.7126(31)	0.8536(19)	0.8569(16)	0.8530(17)
2	1.4939(38)	0.8031(22)	0.8070(17)	0.8025(20)
3	1.3264(38)	0.7615(24)	0.7656(19)	0.7608(21)
4	1.1936(35)	0.7263(25)	0.7307(20)	0.7257(22)
5	1.0856(32)	0.6961(25)	0.7005(20)	0.6968(24)

consistent with the findings of [10]. As previously stated, and in accordance with Ref. [10], we take our preferred values to be those excluding $L/a = 6$ since there is evidence that higher order discretization effects are large for these points, and the uncertainty estimate is more conservative when excluding them. Having excluded the $L/a = 6$ data from our analysis, we compute $R^{(k)}$ for increasing k values, which take us beyond the energy range covered by our data. This is tenable, given that our fit is also constrained by perturbation theory at small u; cf. Fig. 7. The behavior of $R^{(k)}$ with growing k is displayed in Table III, where we also show results for $M/\bar{m}(\mu_0/2)$ [see Eq. (37) below]. We observe that $M/\bar{m}(\mu_0/2)$ remains constant within its error as k increases.

Finally, we can construct the running factor that takes a renormalized quark mass in our chosen (χ)SF scheme at the scale $\mu_0/2$ to the renormalization group invariant quark mass M:

$$\frac{M}{\bar{m}(\mu_0/2)} = \left[\frac{M}{\bar{m}(2^k\mu_0)}\right]\left[\frac{\bar{m}(2^k\mu_0)}{\bar{m}(\mu_0/2)}\right]. \tag{37}$$

The first factor on the rhs can be calculated from

$$\frac{M}{\bar{m}(2^k\mu_0)} = [2b_0\bar{g}^2_{\rm SF}(2^k\mu_0)]^{-d_0/2b_0} \times \exp\left\{-\int_0^{\bar{g}_{\rm SF}(2^k\mu_0)} dx\left[\frac{\tau(x)}{\beta(x)} - \frac{d_0}{b_0 x}\right]\right\}, \tag{38}$$

TABLE III. Mass ratios $R^{(k)}$ and the ratio of RGI to renormalized quark mass at scale $\mu_0/2$, obtained from nonperturbative SSF in χSF at large k values.

k	u_k	$R^{(k)}$-w/o 6	$M/\bar{m}(\mu_0/2)$
5	1.0856(32)	0.6961(25)	1.7514(63)
10	0.7503(19)	0.5899(25)	1.7519(74)
20	0.4664(8)	0.4769(22)	1.7523(81)
30	0.3392(4)	0.4136(19)	1.7522(80)
40	0.2667(3)	0.3716(17)	1.7524(80)

with τ and β given by their perturbative expressions

$$\tau(x) = -x^2[d_0 + d_1x^2 + d_2x^4 + \cdots],$$
$$\beta(x) = -x^3[b_0 + b_1x^2 + b_2x^4 + b_3x^6 + \cdots]. \tag{39}$$

Specifically, we use the two-loop result for $\tau(x)$ (i.e., d_0 and d_1 [44]) and the three-loop result for $\beta(x)$ (i.e., b_0, b_1, and b_2 [45–47]), supplemented by an estimate of b_3 from a fit performed in [21]. The second factor is $R^{(k)}$ of Eq. (36) and it is known nonperturbatively. Having previously shown that the result and its error are practically independent of k, we quote for $k = 10$:

$$\frac{M}{\bar{m}(\mu_0/2)} = 1.7519(74). \tag{40}$$

The above result agrees with the value obtained in the SF-LQCD setup of Ref. [10], $M/\bar{m}(\mu_0/2) = 1.7505(89)$. This is the outcome of a detailed analysis performed by the authors, consisting of four different extrapolation procedures of the $\Sigma_P(u, a/L)$ data, from which estimates of $M/\bar{m}(\mu_0/2)$ are extracted. Their preferred result, quoted here, is obtained from their so-called τ:*global*–FITB* procedure, which consists in performing the continuum extrapolation of $\Sigma_P(u, a/L)$ and the determination of the anomalous dimension $\tau(\bar{g})$ simultaneously. We have also applied this procedure to our data. Outlining the method, we start by rewriting Eq. (35) as

$$\Sigma_P(u, a/L) = \sigma_P(u) + \sum_{n=0}^{2}\rho_n u^n (a/L)^2. \tag{41}$$

Note that terms of $O(a/L)^4$ and higher (i.e., terms with $j \geq 2$) have been dropped from Eq. (35). We have also dropped terms multiplying $(a/L)^2$ of $O(u^3)$ and higher (i.e., b_{n1} terms with $n \geq 3$).

We write the logarithm of $\sigma_P(u)$, in terms of the anomalous dimension τ, as [cf. Eq. (45)]

$$\ln\left(\Sigma_P(u, a/L) - \sum_{n=0}^{2}\rho_n u^n (a/L)^2\right) = -\int_{\sqrt{u}}^{\sqrt{\sigma(u)}} \mathrm{d}x \frac{\tau(x)}{\beta(x)}, \tag{42}$$

where $\sigma(u)$ is the step-scaling function of the renormalized gauge coupling; i.e., for $\bar{g}^2(\mu) = u$, $\sigma(u) = \bar{g}^2(\mu/2)$. For the integrand on the rhs we use the truncated expansions of Eq. (39), where d_0, d_1, b_0, b_1, b_2 are taken from perturbation theory and b_3 from a fit as explained above. Finally, a global fit of the $\Sigma_P(u, a/L)$ data, with free fit parameters ρ_0, ρ_1, ρ_2 and d_2, results to a continuum expression for $\tau(u)$.

Having obtained $\tau(u)$, we can now work out directly $M/\bar{m}(\mu_0/2)$, using Eq. (38), with the scale $\mu_0/2$ in place of $2^k\mu_0$. This gives

$$\frac{M}{\bar{m}(\mu_0/2)} = 1.7517(81). \tag{43}$$

There is excellent agreement with the result of the first procedure, cf. Eq. (40), as well as with the SF-LQCD result of Ref. [10]. We find this particularly encouraging, given the different philosophy of the two procedures. The first one entails a choice of k in Eqs. (36) and (37), which we have taken to be $k = 10$. We have checked the stability of our results for $5 \lesssim k \lesssim 40$. The parametrization of discretization effects included $(a/L)^4$ contributions. In the second procedure, these were taken to be $(a/L)^2$. Although we could have included $(a/L)^4$ terms, we opted to stay as close as possible to the choices made in Ref. [10].

VI. QUARK MASS RUNNING AT LOW ENERGIES

Having computed the running factor to convert the renormalized mass at the scale $\mu_0/2$ to the renormalization group invariant mass, we now turn to the computation of the running factor in the low-energy (GF) regime.

Whereas in the high-energy (SF) regime, we had lattices of extent $L/a = 6, 8, 12$ (and $L/a = 16$ at $u = 2.0120$), in the GF regime our lattices have extent $L/a = 8, 12, 16$, which should improve the continuum extrapolation. In the high-energy regime we found that discretization effects increase as the coupling is increased, and we observe a similar trend in our data in the low-energy regime. It is evident from Fig. 8 that the $(a/L)^2$ coefficient grows with increasing coupling.

The low-energy hadronic scale $\mu_{\rm had}$ is defined by

$$u(\mu_{\rm had}) = 9.25, \tag{44}$$

corresponding to a physical scale $\mu_{\rm had} = 233(8)$ MeV [25]. Since the ratio of the switching scale $\mu_0/2 \sim 2$ GeV to hadronic scale $\mu_{\rm had}$ is not a power of 2, it is inconvenient to carry out the analysis in terms of the step-scaling function $\sigma_P(u)$, which only expresses the quark mass running between consecutive scales μ and $\mu/2$. It is preferable to rely on the mass anomalous dimension $\tau(g)$, related to $\sigma_P(u)$ through

$$\sigma_P(u) = \exp\left[-\int_{\sqrt{u}}^{\sqrt{\sigma(u)}} dg \frac{\tau(g)}{\beta(g)}\right]. \tag{45}$$

Expanding the integrand of the above equation $f(g) \equiv \tau(g)/\beta(g)$ as a power series

$$f(g) = \frac{1}{g}\sum_{k=0} f_k\, g^{2k}, \tag{46}$$

we obtain the following expression for the step-scaling function:

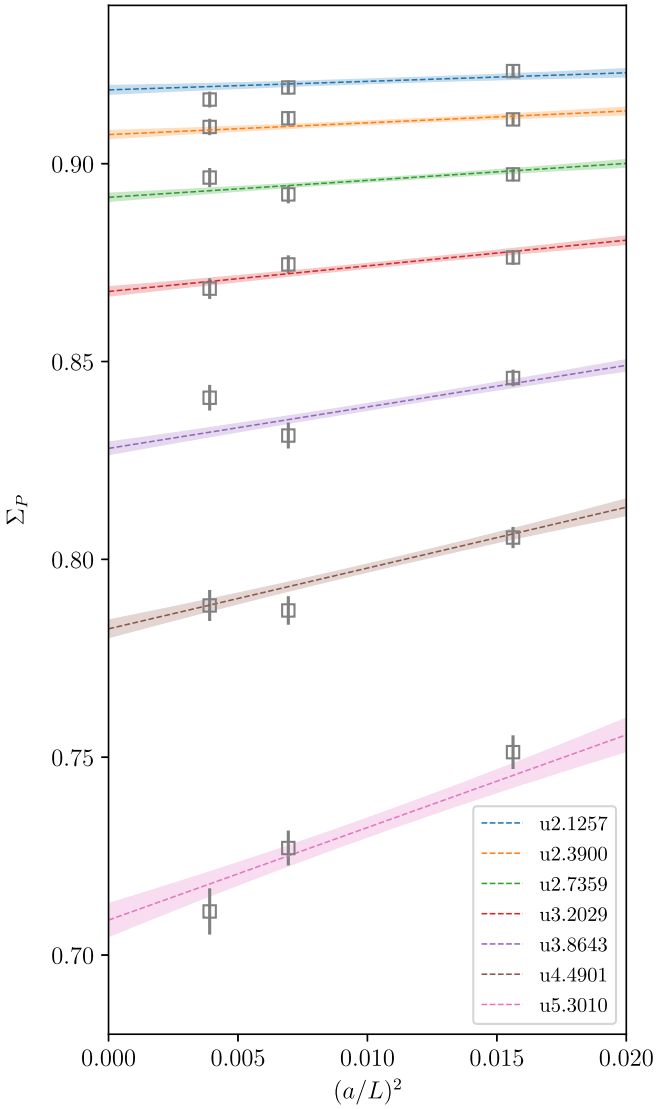

FIG. 8. Results of a global fit to the step-scale data Σ_P in the low-energy regime. The open squares give the raw data while the filled bands are the results returned from the fit at the respective u values. The data points close to the bands are at *approximately* the same u.

$$\ln\, \sigma_P(u) = -\sum_{k=0} f_k \int_{\sqrt{u}}^{\sqrt{\sigma(u)}} dg\, g^{2k-1}. \tag{47}$$

Unlike what we did in the high-energy regime, no input from perturbation theory is introduced in the above expression.

The lattice step-scaling function $\Sigma_P(u, a/L)$ is given as a series expansion in Eq. (35). This can be conveniently rearranged as

$$\Sigma_P(u, a/L) = \sigma_P(u)\left[1 + \sum_{j=1}(a/L)^{2j}\sum_{i=1} d_{ji} u^i\right], \tag{48}$$

resulting to the fit function

$$\ln[\Sigma_P(u,a/L)] = \ln[\sigma_P(u)] + \left[\sum_{j=1}(a/L)^{2J}\sum_{i=1} d_{ji}u^i\right]. \quad (49)$$

Thus the data points $\ln\Sigma_P$ on the lhs are to be fit by the product of the series of $\ln\sigma_P$ of Eq. (47) times the double series with coefficients d_{ji}.

We can vary the number of coefficients f_k parametrizing the continuum form up to a value $k_{\max}$. We also vary the number of coefficients d_{ji} that parametrize lattice artifacts as follows: We consider artifacts that scale as $(a/L)^2$ as well as $(a/L)^4$; i.e., we set $j_{\max} = 2$. For each of the allowed values $j = 1$, 2, we vary the order of the polynomial in u up to $i_{\max}(j)$. Our preferred fit is the one with $k_{\max} = 4$, $i_{\max}(1) = 4$, $i_{\max}(2) = 0$. The fit has a χ^2/d.o.f. of 1.1.

We have checked the stability of our final result to changes in parameters controlling the fit form. We find good agreement in the result using different fit forms, with χ^2/d.o.f. ≈ 1, indicating our data is well represented by and relatively insensitive to the precise details of the fit. This is shown in Fig. 9 for fit forms labeled $(k_{\max}, i_{\max}(1), i_{\max}(2))$. In addition, we can also include/exclude the data at different couplings used in the fits. The authors of [10] excluded data at the two highest couplings $u = 5.8673$ and $u = 6.5489$. Including these couplings gives a consistent result but with somewhat smaller errors. If one instead removes the next high coupling $u = 5.3010$, the data is not sufficiently constraining in the low-energy region and the error increases significantly. The results from these variations are shown using our preferred (4, 4, 0) (and (4, 4, 4)) parametrization in Fig. 9.

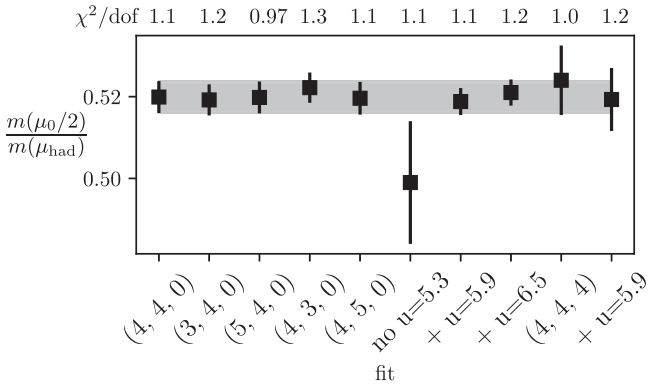

FIG. 9. Stability analysis of the mass running factor in the low-energy regime. The leftmost point shows the result of our preferred fit [Eq. (52)]. The indices $(k_{\max}, i_{\max}(1), i_{\max}(2))$ on the x axis give the number of polynomial terms in u used to parametrize the continuum, $(a/L)^2$, and $(a/L)^4$ dependences respectively. Moving from left to right, the labels "no $u = 5.3$," "$+u = 5.9$," etc. show the effect of removing/adding data at the specified couplings to our preferred (4, 4, 0) fit. The rightmost point shows the effect of adding $u = 5.9$ data to the (4, 4, 4) fit.

After having fit our data for σ_P in both the SF and GF regimes and taken the continuum limit, we find at the switching scale

$$\sigma_{P,\mathrm{SF}}(\mu_0/2) = 0.8951(23), \quad (50)$$

$$\sigma_{P,\mathrm{GF}}(\mu_0/2) = 0.8941(12). \quad (51)$$

The compatibility of these results at the threshold scale $\mu_0/2$, where the definition of the renormalized coupling changes, is yet another indicator of the robustness of our analysis.

Having obtained $f(g)$ from the fit and using the polynomial expression for $\beta(g)$ given in [10], we can reconstruct the function τ and determine

$$\frac{\bar{m}(\mu_0/2)}{\bar{m}(\mu_{\mathrm{had}})} = 0.5199(39), \quad (52)$$

which can be compared with the result from [10], $\frac{\bar{m}(\mu_0/2)}{\bar{m}(\mu_{\mathrm{had}})} = 0.5226(43)$.

VII. CONCLUSION

We have analyzed the ensembles generated for the computation of the RG running of the quark mass in $N_f = 3$ massless QCD (with SF boundaries) [10], imposing chirally rotated Schrödinger functional boundary conditions on the valence quarks. The data spans a few orders of magnitude, allowing a completely nonperturbative determination of the mass running function between the hadronic and very high-energy scales, where contact with fixed-order perturbation theory can be made. Our computations are characterized by two different definitions of the renormalized gauge coupling below and above an energy threshold (switching scale) of ∼2 GeV. This results to some differences in the computational strategies in the low- and high-energy regimes.

In order to recover all the symmetries of QCD in the continuum limit, we have performed the required nonperturbative tuning of the boundary counterterm z_{f} of the χSF valence quark. The critical value κ_{c} of the mass tuning parameter κ is taken from Ref. [10].

We computed in both high- and low-energy regions the ratio Z_S/Z_P and the ratio of step-scaling functions Σ_S/Σ_P. For the former we find that results match smoothly with one-loop PT in the high-energy regime. We also find consistency with determinations based on Ward identities in the low-energy regime. The latter provides an important diagnostic check for the validity of our fit forms, and we find that the one-loop subtraction is effective at removing the leading lattice artifacts in this quantity. The ratio of step-scaling functions Σ_S/Σ_P provides a second diagnostic check of our setup. The continuum limit step-scaling

functions σ_S and σ_P are expected to be equal in a χSF setup. We confirm that the ratio Σ_S/Σ_P fulfills this expectation.

Our main result consists in the computation of the step-scaling function σ_P (equivalently τ/β) from hadronic to electroweak energy scales. In the high-energy regime, we computed the quark mass running factor from the switching scale to the RG-invariant definition of the quark mass. In the low-energy regime, we computed the mass running factor from the hadronic scale $\mu_{\rm had}$ to the switching scale. Putting these results together we obtain the total running factor,

$$\frac{M}{\bar{m}(\mu_{\rm had})} = 0.9108(78), \tag{53}$$

from Eq. (40) and

$$\frac{M}{\bar{m}(\mu_{\rm had})} = 0.9107(80) \tag{54}$$

from Eq. (43). These can be compared to the SF-LQCD result from Ref. [10], namely $M/\bar{m}(\mu_{\rm had}) = 0.9148(88)$, obtained on the same configuration ensembles.

Our results for the mass running factors are consistent with the findings of [10]. The two formulations are formally equivalent in the continuum, but are obtained from two different regularizations of the valence quark action. Their compatibility is a nontrivial check of universality of the two lattice theories.

Having validated our setup quantitatively lays the groundwork for studies of other bilinear operators, such as the tensor which, without an improvement scheme in SF, suffers $O(a)$ artifacts. Work towards obtaining automatically improved tensor matrix elements is under way; see Ref. [48] for preliminary results. Similar advantages are expected for more complicated four-quark operators, like those used in studies of kaon mixing beyond the Standard Model. The strategy for computing automatically $O(a)$-improved B_K matrix elements, including beyond the Standard Model contributions, in a χSF renormalization scheme, has been outlined in Refs. [14,15].

ACKNOWLEDGMENTS

We wish to thank Patrick Fritzsch, Carlos Pena, David Preti, and Alberto Ramos for their help. This work is partially supported by INFN and CINECA, as part of research project of the QCDLAT INFN initiative. We acknowledge the Santander Supercomputacion support group at the University of Cantabria which provided access to the Altamira Supercomputer at the Institute of Physics of Cantabria (IFCA-CSIC). We also acknowledge support by the Poznan Supercomputing and Networking Center (PSNC) under the project with Grant No. 466. A. L. acknowledges support by the U.S. Department of Energy under Grant No. DE-SC0015655.

APPENDIX A: DETERMINATION OF $z_{\rm f}$

To obtain automatic $O(a)$ improvement we tune non-perturbatively the boundary counterterm $z_{\rm f}$ in order to satisfy Eq. (11). This is done at the $\kappa_{\rm c}$ values obtained in Ref. [10] with SF boundary conditions for the quark fields. We use an iterative procedure. Starting from an initial guess $(z_{\rm f}^{(0)}, s^{(0)})$, for $z_{\rm f}$ and $s \equiv \frac{\partial}{\partial z_{\rm f}} g_A^{ud}(T/2)$, we compute $g_A^{ud}(T/2)[z_{\rm f}] \equiv g_A^{ud}[z_{\rm f}]$ for a given gauge field ensemble. We then update the values

$$z_{\rm f}^{(i+1)} = z_{\rm f}^{(i)} - g_A^{ud}[z_{\rm f}^{(i)}]/s^{(i)} \tag{A1}$$

$$s^{(i+1)} = (g_A^{ud}[z_{\rm f}^{(i+1)}] - g_A^{ud}[z_{\rm f}^{(i)}])/(z_{\rm f}^{(i+1)} - z_{\rm f}^{(i)}), \tag{A2}$$

where $g_A^{ud}[z_{\rm f}^{(i+1)}]$ is computed after (A1) in order to update the slope in (A2). As convergence criterion we require that the correlator be zero within statistical errors,

$$|g_A^{ud}(T/2)| < \delta g_A^{ud}(T/2). \tag{A3}$$

As an initial starting guess we take the $O(g_0^2)$ perturbative result [3] for $z_{\rm f}^{(0)} = 1 + g_0^2 C_F \times 0.16759(1)$. The initial guess for the slope $s^{(0)}$ was determined empirically by measuring $g_A^{ud}[z_{\rm f}]$ for a few $z_{\rm f}$ values near $z_{\rm f}^{(0)}$ on a single ensemble, from which we obtained $s^{(0)} = -2.3$. In practice the slope is found to be a slowly varying function of g_0^2 (cf. Fig. 10) and the termination of the algorithm does not depend sensitively on its initial value. Because we are working in a narrow range around the final value of $z_{\rm f}$, the correlator $g_A^{ud}[z_{\rm f}]$ varies nearly linearly with $z_{\rm f}$.

For the computation of g_A^{ud} the algorithm is first run in a low-precision mode using 1000 configurations, and when the convergence criterion (A3) is satisfied, it switches to a high-precision mode using the full ensemble. The new starting values are the $z_{\rm f}$ and the slope estimates of the

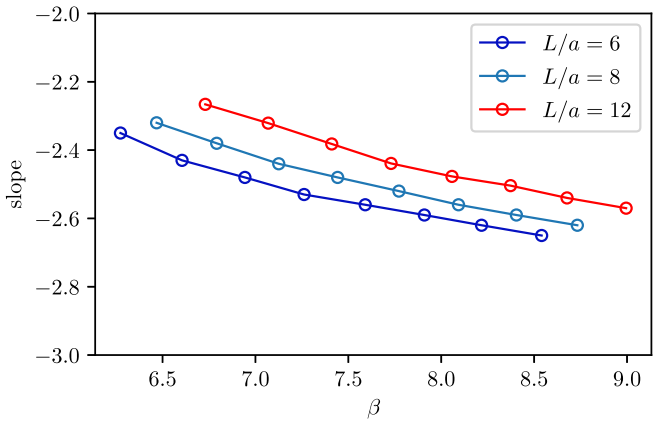

FIG. 10. The slope $\frac{\partial}{\partial z_{\rm f}} g_A^{ud}(T/2)$ as a function of β, with varying L/a, in the high-energy range.

low-precision run. The values of $g_A^{ud}[z_f]$ for successive z_f estimates are highly correlated, so the slopes are determined precisely and the algorithm terminates quickly.

Results for both the SF and GF ensembles are shown in Fig. 1. We see that z_f varies smoothly with g_0^2 in each energy regime (SF and GF). Compared to the $O(g_0^2)$ perturbative result, it clearly has sizable contributions from higher orders. The results for z_f could turn out to be useful in future studies of χSF-LQCD with $N_f = 3$. For this reason we present detailed results on the quantities relevant to this tuning in a separate Appendix D.

APPENDIX B: RETUNING κ_c

The value of κ_c tuned in the χSF regularization differs from the value tuned in the SF one by $O(a)$ lattice artifacts. However, when physical observables in the χSF setup are computed using these two κ_c values, the two determinations differ only by $O(a^2)$ lattice artifacts [3]. In this Appendix we check that physical results computed with z_f tuned with κ_c fixed at the SF values of Ref. [10] are compatible to those obtained when z_f and κ_c are tuned simultaneously with an iterative procedure in the χSF setup.

Our test consists in computing the SSFs of the pseudoscalar and scalar operators (19) and (20), at a single value of the renormalized coupling, $u_{SF}(\mu_0) = 2.012$, for which an extra fine lattice with $L/a = 16$ is available. Considerations based on $O(a)$ improvement in Ref. [9] imply that the quark mass depends weakly on z_f. This suggests an iterative procedure, in which either z_f or κ_c is tuned in alternation, while the other parameter is held fixed. The output of a tuning stage (say, z_f) is thus kept fixed in the successive stage, in which the other parameter (say κ_c) is being tuned. As we do not expect the quark mass to change appreciably with small variations of z_f, the overall process should converge rapidly.

TABLE IV. Percentage variation of z_f and κ_c (for $u_{SF} = 2.012$ ensembles) between the values tuned as in Appendix A (denoted by a superscript SF) and those tuned according to the present procedure (denoted by a superscript χSF).

L/a	N_{conf}	$\frac{z_f^{\chi SF} - z_f^{SF}}{z_f^{\chi SF}} \times 100$	$\frac{\kappa_c^{\chi SF} - \kappa_c^{SF}}{\kappa_c^{\chi SF}} \times 100$
6	5000	0.94	0.06
8	5000	0.36	0.02
12	3000	0.31	0.01
16	4604	0.19	0.005

This procedure is displayed in Fig. 11. The first stage consists in tuning of z_f with κ_c held fixed at the SF value of Ref. [10]. Essentially this is what is described in Appendix A. The convergence criterion is met after three iterations (step 3 in Fig. 11). Then the second stage begins, where κ_c is tuned with z_f held fixed. This is analogous to what is done in Appendix A, with z_f replaced by κ_c: the initial guesses for κ_c and the slope $\frac{\partial(mL)}{\partial\kappa}$ are taken from Ref. [10] and Appendix B of Ref. [9] respectively. The algorithm first runs in low precision mode and then in high precision mode; after three iterations (step 6 in Fig. 11) the PCAC mass is naught within statistical precision. Note that in practice we tune the bare quark mass m_0 using the slope $\frac{\partial(mL)}{\partial(m_0 L)}$ and then we convert it to $\kappa = \frac{1}{2m_0+8}$. We prefer this because m is linear in m_0. See Ref. [9] for more details.

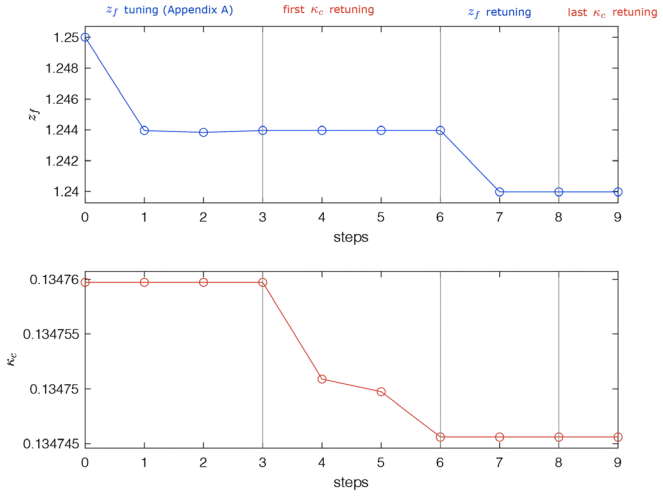

FIG. 11. Simultaneous tuning of z_f and κ at $u_{SF} = 2.012$ and lattice volume $L/a = 12$. On the x axis we enumerate the iteration step of the overall tuning procedure; the vertical dotted lines indicate the end of a tuning stage. Each tuning stage ends when the appropriate convergence criterion is met.

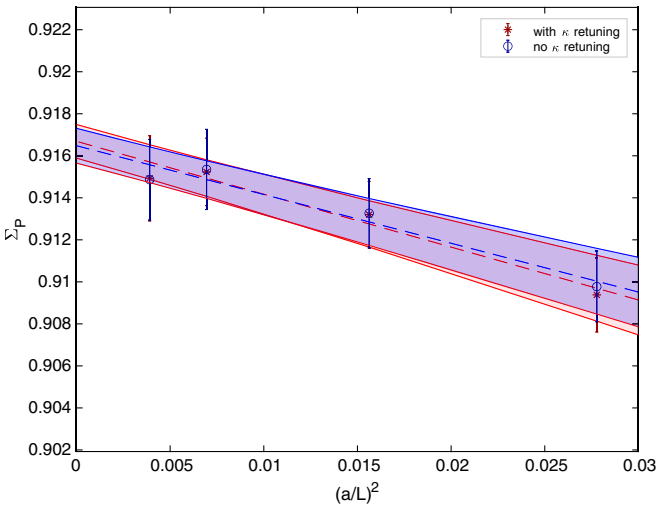

FIG. 12. $\Sigma_P^{\chi SF}$ vs $(a/L)^2$ at $u_{SF} = 2.012$. In red we show data and related fits computed with the simultaneous tuning of z_f and κ_c; in blue, those computed without κ_c retuning.

We can carry on by retuning z_f while keeping κ_c fixed to its new value; this is stage 3 of our procedure. The new initial guesses for z_f and the slope $\frac{\partial}{\partial z_f} g_A^{ud}(T/2)$ are the output of the previous z_f tuning (stage 1). We alternate the two tuning procedures until both parameters remain stable within their errors.

Looking at the percentage variations of z_f and κ_c after their retuning, we see that both of them have not changed considerably: the variation of z_f is less than 1 percent for all lattice volumes and that of κ_c is smaller than 1 per mil. The values are given in Table IV.

We finally compare results for $\Sigma_P^{\chi\mathrm{SF}}$, obtained with and without retuning of κ_c. In Fig. 12 $\Sigma_P^{\chi\mathrm{SF}}$ is plotted against $(a/L)^2$ at the renormalized squared coupling $u_{\mathrm{SF}} = 2.012$. The figure shows that the two sets of data overlap strongly, both at finite lattice spacing and in the continuum.

We conclude that the tuning procedure can be stopped after completion of the first stage (step 3 in Fig. 11), as described in Appendix A, without loss of precision for the quantities of interest.

APPENDIX C: THE EFFECT OF d_s

We compare the results for $\Sigma_P^{\chi\mathrm{SF}}$ obtained with the tree-level value of d_s to those obtained with the one-loop result. We perform the test at $u_{SF} = 2.0120$, where the difference between the tree-level and one-loop estimates of d_s is the biggest possible in our high-energy (SF) range: $(d_s^{\text{1-loop}} - d_s^{\text{tree}}) = d_s^{(1)} \times 2.0120 = 0.0016(8)$. As expected and shown in Fig. 13, the data points obtained with the two d_s estimates overlap completely.

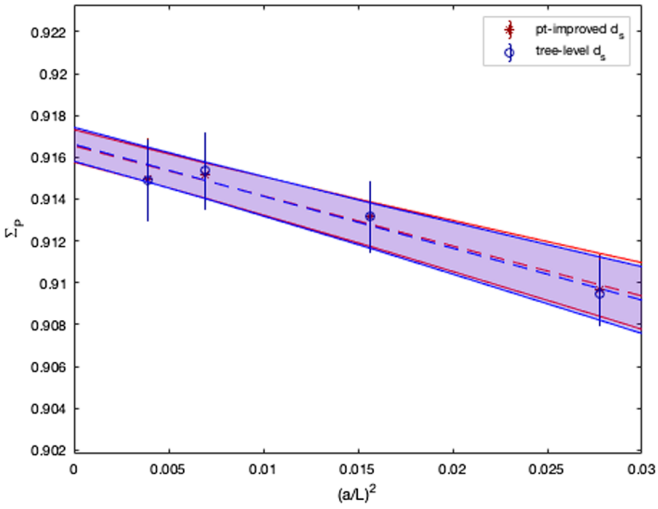

FIG. 13. $\Sigma_P^{\chi\mathrm{SF}}$ vs $(a/L)^2$ at $u_{\mathrm{SF}} = 2.012$. In red we show data and related fits computed with d_s^{tree}; in blue, those computed with $d_s^{\text{1-loop}}$.

APPENDIX D: SIMULATION DETAILS

In Tables V and VI we collect numerical details of our simulations in the SF and GF regimes, respectively.

TABLE V. The first column refers to the values of the squared renormalized gauge coupling $\bar{g}^2(\mu) = u$ in the SF energy region; columns 2 to 5 display the relevant bare lattice parameters corresponding to u; column 6 shows the number of gauge field configurations used for the measurements. The last three columns contain the output of the tuned z_f and the final values of g_A^{ud} and $\partial g_A^{ud}/\partial z_f$.

u	L/a	β	κ_c	c_{sw}	N_{ms}	g_A^{ud}	$\partial g_A^{ud}/\partial z_f$	z_f
1.110000	6	8.5403	0.13233610	1.233045285565058	5000	3.34×10^{-7} +/− 0.000529	−2.6411749	1.18588709299
1.110000	8	8.7325	0.13213380	1.224666388699756	5000	-6.87×10^{-7} +/− 0.000397	−2.6152159	1.18374688510
1.110000	12	8.9950	0.13186210	1.214293680665697	2769	1.89×10^{-6} +/− 0.000348	−2.5572039	1.17624612625
1.184460	6	8.2170	0.13269030	1.248924515099129	5000	-1.33×10^{-5} +/− 0.000571	−2.6258675	1.19427949923
1.184460	8	8.4044	0.13247670	1.239426196162344	5000	7.34×10^{-6} +/− 0.000419	−2.5982674	1.19224223013
1.184460	12	8.6769	0.13217153	1.22701700000000	2476	1.12×10^{-7} +/− 0.000403	−2.5383549	1.18417905314
1.265690	6	7.9091	0.13305720	1.266585617959733	5000	7.17×10^{-6} +/− 0.000598	−2.6054349	1.20212085045
1.265690	8	8.0929	0.13283120	1.255711356539447	5000	-9.56×10^{-7} +/− 0.000456	−2.5579952	1.20026752592
1.265690	12	8.3730	0.13249231	1.24095900000000	2729	2.36×10^{-8} +/− 0.000400	−2.5034648	1.19163887560
1.362700	6	7.5909	0.13346930	1.288146969458134	5000	-8.57×10^{-7} +/− 0.000656	−2.5642314	1.21157164130
1.362700	8	7.7723	0.13322830	1.275393611340024	5000	-1.20×10^{-6} +/− 0.000485	−2.5192879	1.21009426577
1.362700	12	8.0578	0.13285365	1.25770900000000	2448	1.20×10^{-6} +/− 0.000456	−2.4722959	1.20100624217
1.480800	6	7.2618	0.13393370	1.315030958783770	5000	1.37×10^{-6} +/− 0.000709	−2.5311118	1.22119155568
1.480800	8	7.4424	0.13367450	1.299622821237046	5000	2.26×10^{-6} +/− 0.000538	−2.4850676	1.22025587648
1.480800	12	7.7299	0.13326353	1.278252758659668	2711	-5.95×10^{-7} +/− 0.000463	−2.4422897	1.21049262680
1.617300	6	6.9433	0.13442200	1.346919223092444	5000	2.77×10^{-6} +/− 0.000786	−2.4829699	1.23119560164
1.617300	8	7.1254	0.13414180	1.327878356622864	5000	1.47×10^{-7} +/− 0.000582	−2.4485296	1.23052937460
1.617300	12	7.4107	0.13369922	1.30220600000000	2535	4.55×10^{-8} +/− 0.000509	−2.3828505	1.22067806449

(Table continued)

TABLE V. *(Continued)*

u	L/a	β	κ_c	c_{sw}	N_{ms}	g_A^{ud}	$\partial g_A^{ud}/\partial z_f$	z_f
1.794300	6	6.6050	0.13498290	1.389385004928746	5000	$-2.33 \times 10^{-6} +/- 0.000859$	−2.4255593	1.24169304397
1.794300	8	6.7915	0.13467650	1.364706438701718	5000	$-1.19 \times 10^{-5} +/- 0.000638$	−2.3657177	1.24218454960
1.794300	12	7.0688	0.13420891	1.333551296494656	2339	$-7.03 \times 10^{-6} +/- 0.000592$	−2.3034246	1.23170004013
2.012000	6	6.2735	0.13557130	1.442967721668930	5000	$-8.02 \times 10^{-6} +/- 0.000971$	−2.3627021	1.25238467445
2.012000	8	6.4680	0.13523620	1.409845308468962	5000	$-3.40 \times 10^{-7} +/- 0.000706$	−2.3251048	1.25331910626
2.012000	12	6.7299	0.13475973	1.372481791156670	3000	$-1.44 \times 10^{-6} +/- 0.000603$	−2.2547920	1.24396571640
2.012000	16	6.9346	0.13441209	1.34788873527000	4604	$3.14 \times 10^{-6} +/- 0.000340$	−2.2150346	1.23527136701

TABLE VI. The first column refers to the values of the squared renormalized gauge coupling $\bar{g}^2(\mu) = u$ in the GF energy region; columns 2 to 5 display the relevant bare lattice parameters corresponding to u; column 6 shows the number of gauge field configurations used for the measurements. The last three columns contain the output of the tuned z_f and the final values of g_A^{ud} and $\partial g_A^{ud}/\partial z_f$.

u	L/a	β	κ_c	c_{sw}	N_{ms}	g_A^{ud}	$\partial g_A^{ud}/\partial z_f$	z_f
2.125700	8	5.3715	0.13362120	1.259364773796311	5000	$4.06 \times 10^{-6} +/- 0.000534$	−2.4642129	1.22654269651
2.125700	12	5.5431	0.13331407	1.244237155112229	2001	$-1.15 \times 10^{-6} +/- 0.000285$	−2.3724251	1.21985757706
2.125700	16	5.7000	0.13304840	1.232057931661424	8000	$1.70 \times 10^{-6} +/- 0.000217$	−2.2984404	1.21389574489
2.390000	8	5.0710	0.13421678	1.291712997425573	5000	$-2.46 \times 10^{-6} +/- 0.000593$	−2.3937509	1.24245430325
2.390000	12	5.2425	0.13387635	1.272228757209511	2001	$1.77 \times 10^{-5} +/- 0.000311$	−2.3527260	1.23476121175
2.390000	16	5.4000	0.13357851	1.256705230332892	8000	$-1.26 \times 10^{-6} +/- 0.000261$	−2.2530349	1.22758469820
2.735900	8	4.7649	0.13488555	1.335350323996506	5001	$-2.82 \times 10^{-6} +/- 0.000687$	−2.3249628	1.25947416858
2.735900	12	4.9387	0.13450761	1.308983384364439	2001	$1.83 \times 10^{-5} +/- 0.000442$	−2.2719935	1.25193714648
2.735900	16	5.1000	0.13416889	1.288203306487197	5001	$-1.65 \times 10^{-6} +/- 0.000297$	−2.1546738	1.24351820011
3.202900	8	4.4576	0.13560675	1.395741031275910	5001	$6.60 \times 10^{-5} +/- 0.000793$	−2.3080103	1.27801540556
3.202900	12	4.6347	0.13519986	1.358462476494125	2001	$4.79 \times 10^{-6} +/- 0.000520$	−2.1513773	1.27063136963
3.202900	16	4.8000	0.13482139	1.329646151978636	5001	$3.06 \times 10^{-7} +/- 0.000360$	−2.0625697	1.26149028258
3.864300	8	4.1519	0.13632589	1.482418125298923	5001	$3.73 \times 10^{-7} +/- 0.000980$	−2.1399699	1.29722920690
3.864300	12	4.3317	0.13592664	1.427424655158656	2001	$-9.72 \times 10^{-7} +/- 0.000617$	−2.0302207	1.29144247047
3.864300	16	4.5000	0.13552582	1.386110343557152	5001	$-1.38 \times 10^{-6} +/- 0.000427$	−1.9484240	1.28199124254
4.490100	8	3.9479	0.13674684	1.563885414775983	5001	$1.64 \times 10^{-4} +/- 0.001100$	−2.0493154	1.30786594013
4.490100	12	4.1282	0.13640300	1.490702297580152	2001	$-1.31 \times 10^{-5} +/- 0.000713$	−1.9429389	1.30582505718
4.490100	16	4.3000	0.13600821	1.436199798821361	5001	$-1.53 \times 10^{-5} +/- 0.000493$	−1.8420700	1.29622706156
5.301000	8	3.7549	0.13701929	1.668369108400627	5001	$-8.19 \times 10^{-6} +/- 0.001380$	−1.9545399	1.31461240780
5.301000	12	3.9368	0.13679805	1.569056010619204	2001	$2.31 \times 10^{-5} +/- 0.000831$	−1.8037352	1.31770290718
5.301000	16	4.1000	0.13647301	1.500935714848465	5001	$-2.01 \times 10^{-5} +/- 0.000717$	−1.7111716	1.31005410303
5.867300	8	3.6538	0.13707221	1.738234164347418	5001	$-3.05 \times 10^{-5} +/- 0.001560$	−1.8809782	1.31487229203
5.867300	12	3.8333	0.13696774	1.621966539608638	5001	$5.56 \times 10^{-5} +/- 0.000921$	−1.7457623	1.32327345473
5.867300	16	4.0000	0.13668396	1.540714371185832	4602	$-2.24 \times 10^{-5} +/- 0.000654$	−1.6560183	1.31588724381
6.548900	8	3.5565	0.13703245	1.818951161611082	5001	$-3.29 \times 10^{-5} +/- 0.001830$	−1.8016743	1.31531748561
6.548900	12	3.7354	0.13708263	1.680901952205217	5001	$2.42 \times 10^{-6} +/- 0.001080$	−1.6027921	1.32886731276
6.548900	16	3.9000	0.13687202	1.586881030973021	4600	$-5.17 \times 10^{-7} +/- 0.000737$	−1.5210420	1.32248784097

[1] S. Sint, Nucl. Phys. **B847**, 491 (2011).

[2] M. Lüscher, S. Sint, R. Sommer, and P. Weisz, Nucl. Phys. **B478**, 365 (1996).

[3] M. Dalla Brida, S. Sint, and P. Vilaseca, J. High Energy Phys. 08 (2016) 102.

[4] S. Sint and B. Leder, Proc. Sci., LATTICE2010 (**2010**) 265 [arXiv:1012.2500].

[5] R. Sommer, Nucl. Phys. **B411**, 839 (1994).

[6] J. Lopez, K. Jansen, D. Renner, and A. Shindler, Nucl. Phys. **B867**, 567 (2013).

[7] J. Lopez, K. Jansen, D. Renner, and A. Shindler, Nucl. Phys. **B867**, 609 (2013).
[8] S. Capitani, M. Lüscher, R. Sommer, and H. Wittig, Nucl. Phys. **B544**, 669 (1999); **B582**, 762(E) (2000).
[9] M. Dalla Brida, T. Korzec, S. Sint, and P. Vilaseca, Eur. Phys. J. C **79**, 23 (2019).
[10] I. Campos, P. Fritzsch, C. Pena, D. Preti, A. Ramos, and A. Vladikas, Eur. Phys. J. C **78**, 387 (2018).
[11] P. Dimopoulos, G. Herdoiza, F. Palombi, M. Papinutto, C. Pena, A. Vladikas, and H. Wittig (ALPHA Collaboration), J. High Energy Phys. 05 (2008) 065.
[12] P. Dimopoulos, G. Herdoíza, M. Papinutto, C. Pena, D. Preti, and A. Vladikas (ALPHA Collaboration), Eur. Phys. J. C **78**, 579 (2018).
[13] P. Dimopoulos, H. Simma, and A. Vladikas, J. High Energy Phys. 07 (2009) 007.
[14] P. V. Mainar, M. Dalla Brida, and M. Papinutto, Proc. Sci., LATTICE2015 (**2016**) 252.
[15] I. Campos, M. Dalla Brida, G. M. de Divitiis, A. Lytle, M. Papinutto, and A. Vladikas, Proc. Sci., LATTICE2019 (**2019**) 202 [arXiv:1910.01898].
[16] I. C. Plasencia, M. D. Brida, G. M. de Divitiis, A. Lytle, M. Papinutto, L. Pirelli, and A. Vladikas, Proc. Sci., LATTICE2021 (**2021**) 364 [arXiv:2111.15384].
[17] R. Frezzotti and G. Rossi, J. High Energy Phys. 08 (2004) 007.
[18] S. Sint, arXiv:hep-lat/0702008.
[19] M. Dalla Brida, P. Fritzsch, T. Korzec, A. Ramos, S. Sint, and R. Sommer (ALPHA Collaboration), Phys. Rev. Lett. **117**, 182001 (2016).
[20] M. Dalla Brida, P. Fritzsch, T. Korzec, A. Ramos, S. Sint, and R. Sommer (ALPHA Collaboration), Phys. Rev. D **95**, 014507 (2017).
[21] M. Dalla Brida, P. Fritzsch, T. Korzec, A. Ramos, S. Sint, and R. Sommer (ALPHA Collaboration), Eur. Phys. J. C **78**, 372 (2018).
[22] M. Lüscher, R. Narayanan, P. Weisz, and U. Wolff, Nucl. Phys. **B384**, 168 (1992).
[23] M. Luscher, R. Sommer, P. Weisz, and U. Wolff, Nucl. Phys. **B413**, 481 (1994).
[24] P. Fritzsch and A. Ramos, J. High Energy Phys. 10 (2013) 008.
[25] M. Bruno, M. Dalla Brida, P. Fritzsch, T. Korzec, A. Ramos, S. Schaefer, H. Simma, S. Sint, and R. Sommer (ALPHA Collaboration), Phys. Rev. Lett. **119**, 102001 (2017).
[26] K. G. Wilson, Phys. Rev. D **10**, 2445 (1974).
[27] B. Sheikholeslami and R. Wohlert, Nucl. Phys. **B259**, 572 (1985).
[28] N. Yamada *et al.* (JLQCD and *CP*-PACS Collaborations), Phys. Rev. D **71**, 054505 (2005).
[29] S. Sint and P. Weisz, Nucl. Phys. **B502**, 251 (1997).
[30] A. Bode, U. Wolff, and P. Weisz (Alpha Collaboration), Nucl. Phys. **B540**, 491 (1999).
[31] M. Lüscher and P. Weisz, Phys. Lett. **158B**, 250 (1985).
[32] J. Bulava and S. Schaefer, Nucl. Phys. **B874**, 188 (2013).
[33] P. Vilaseca (private communication).
[34] S. Aoki, R. Frezzotti, and P. Weisz, Nucl. Phys. **B540**, 501 (1999).
[35] G. P. Lepage, LSQFIT (version 11.7), https://github.com/gplepage/lsqfit.
[36] G. P. Lepage, GVAR (version 11.9.1), https://github.com/gplepage/gvar.
[37] U. Wolff, Comput. Phys. Commun. **156**, 143 (2004); **176**, 383(E) (2007).
[38] G. M. de Divitiis, P. Fritzsch, J. Heitger, C. C. Köster, S. Kuberski, and A. Vladikas (ALPHA Collaboration), Eur. Phys. J. C **79**, 797 (2019).
[39] J. Heitger, F. Joswig, and A. Vladikas (ALPHA Collaboration), Eur. Phys. J. C **80**, 765 (2020).
[40] J. Heitger, F. Joswig, P. L. J. Petrak, and A. Vladikas, Eur. Phys. J. C **81**, 606 (2021).
[41] M. Bruno *et al.*, J. High Energy Phys. 02 (2015) 043.
[42] D. Mohler, S. Schaefer, and J. Simeth, EPJ Web Conf. **175**, 02010 (2018).
[43] M. Dalla Brida, A. Mellini, M. Papinutto, F. Scardino, and P. Vilaseca (ALPHA Collaboration) (to be published).
[44] S. Sint and P. Weisz (ALPHA Collaboration), Nucl. Phys. **B545**, 529 (1999).
[45] W. E. Caswell, Phys. Rev. Lett. **33**, 244 (1974).
[46] D. R. T. Jones, Nucl. Phys. **B75**, 531 (1974).
[47] A. Bode, P. Weisz, and U. Wolff (ALPHA Collaboration), Nucl. Phys. **B576**, 517 (2000); **B608**, 481(E) (2001); **B600**, 453(E) (2001).
[48] I. C. Plasencia, M. D. Brida, G. M. de Divitiis, A. Lytle, M. Papinutto, L. Pirelli, and A. Vladikas, Proc. Sci., LATTICE2021 (**2021**) 253 [arXiv:2111.15325].